Pairing Combustion Experiments and Thermogravimetric Analysis to Uncover Timescales Controlling Cellulose Ignition and Burnout in a Hencken Burner

Parvaneh Motiei[a], Matteo Pecchi[b], James L. Adair[b], Jillian L. Goldfarb[b]
Jacqueline O'Connor[a,*]

[a] Mechanical Engineering, Pennsylvania State University, University Park, PA USA

[b] Biological and Environmental Engineering, Cornell University, Ithaca, NY USA

* Corresponding author: 111 Research East Building, University Park, PA 16802, jxo22@psu.edu

Abstract

Solid biomass fuels are potential components of several industrial and power-generation decarbonization pathways. Despite considerable literature that documents the fuel properties of lignocellulosic biomass, the fundamental combustion characteristics of biomass constituents are not well understood. We tackle this knowledge gap by analyzing the combustion properties of cellulose (a key biomass component) in a Hencken burner across various temperature and oxygen mole fractions of the oxidizer gases. Combustion data are compared with results from thermogravimetric analysis (TGA) and scaling analyses to reveal two rate-controlling timescales in the ignition of cellulose: devolatilization time and volatile ignition delay time. TGA shows that the devolatilization time is only a function of temperature and occurs on a considerably shorter timescale than oxidation. Hencken burner experiments show that ignition delay time is highly sensitive to temperature; at very low levels of oxygen in the oxidizer gas (mole fractions of 0.01-0.04), the ignition delay time is sensitive to oxygen mole fraction, but this sensitivity disappears at higher oxygen levels. Burnout time is the least sensitive parameter investigated. The combination of experiments and chemical kinetic simulations begins to explain the ignition behavior of the volatiles from cellulose decomposition and lays groundwork for future research to address uncertainties in quantifying the kinetics of cellulose ignition. Finally, this combined combustion-fuel science study raises serious doubts about the use of combustion indices and TGA-calculated properties to predict the true combustion behavior of biomass.

Keywords: Cellulose, Ignition, Devolatilization, Biomass combustion, Hencken burner

Novelty and Significance: We address a gap in knowledge about the combustion properties of cellulose, a critical building block of lignocellulosic biomass, through the use of a Hencken burner experiment by varying the temperature and oxygen mole fraction of the oxidizer. Simultaneous CH* chemiluminescence and particle image velocimetry are used to measure ignition delay and burnout times, and a rigorous uncertainty analysis is performed to provide validation-quality data. Combustion data are compared with results from thermogravimetric analysis (TGA) and computational scaling analyses to reveal two rate-controlling timescales in the ignition of cellulose: devolatilization time and volatile ignition delay time. The combustion and TGA data are compared in a new and rigorous manner, providing sound links between methods used in the two fields of fuel science and combustion.

Author contributions:

P.M. – designed experiment, obtained data, data analysis, wrote manuscript

M.P. – obtained data, data analysis, edited manuscript

J.A. – data analysis, edited manuscript

J.G. – designed experiment, data analysis, edited manuscript

J.O. – chemical analysis, designed experiment, edited manuscript

1 Introduction

Decarbonization will likely require the integration of biomass-based fuels into conventional power- and heat-generation systems to reduce net greenhouse gas emissions [1]. Direct combustion of biomass alters the performance of furnaces and pulverized solid fuel burners due to biomass' higher particle ignition and lower burnout temperatures, and weaker flame stability as compared to fossil fuels [2–4]. As such, a comprehensive understanding of biomass combustion behavior is necessary [5,6]. However, the current renewable fuel literature relies heavily upon thermogravimetric analysis (TGA) to investigate "combustion characteristics" of biofuels [7–9]. Since TGA heating conditions are orders of magnitude slower than an industrial combustor, it is not clear if TGA can mimic the true combustion characteristics of fuels in real apparatuses [10].

Biomass combusts in three stages: endothermic drying and devolatilization, combustion of volatiles, and exothermic oxidation of char to gaseous combustion products and solid ash [11]. Since the endothermic drying step can compromise ignition and reduce the combustion temperature for high-moisture feedstocks, biomass is often dried in a separate pre-processing step [12]. Biomass combustion is typically characterized by ignition delay time [13–19], devolatilization time [16,17,20], burn-out time [16,20], and ignition temperature [15,17,20]. Biomass combustion is tested using a variety of combustion devices, including Hencken burners [21–24], McKenna burners [18,19,25,26], drop tube furnaces [20,27,28], pellet, single-particle, or briquette burners [29–32], and packed bed reactors [33,34]. Studies focus on the influence of the biomass type [35,36], oxidizing environment composition, diluent agent, surrounding gas temperature [13,15,17,18], and moisture content [14,16] on combustion characteristics of biomass. Combustion experiments show that biomass ignition delay time and devolatilization time are inversely proportional to the co-flow temperature and the O_2 mole fraction, where the extent of O_2 influence depends on the ignition mode [17,18]. Regardless of diluent gas composition, the flame and particle surface temperatures increase at higher O_2 mole fractions in the oxidizer. The burnout time is shorter at higher O_2 mole fractions, as the O_2 mass flux accelerates the oxidation of volatiles, which releases heat that subsequently enhances devolatilization, ignition, and combustion. Replacing N_2 in air with other diluents affects the ignition behavior. For instance, using CO_2 instead of N_2 in oxy-fuel applications lowers the burning rate of the volatile flame as well as the particle temperatures. This change lengthens the burnout and devolatilization times due, in part, to the larger heat capacity of CO_2 and the lower binary diffusivity of O_2 in CO_2 [3,15].

The impact of O_2 concentrations and co-flow temperature on ignition behavior have been investigated independently, as is done in this study. Shan et al. [17] experimentally investigated the impact of co-flow velocity and temperature on the ignition process of a single biomass pellet in an electrically heated tube furnace. At the same gas flow rate and co-flow temperature, varying the O_2 mole fraction affected the ignition delay time less significantly than varying the co-flow temperature. The effects of co-flow velocity on ignition delay time of biomass were smaller than co-flow temperature and O_2 mole fraction. Furthermore, because of a sharp increase of the flame temperature during volatile combustion, the co-flow temperature was not a determining factor in the volatile burnout time. In another study, Simoes et al. [18] explored the effect of co-flow temperature and O_2 mole fraction on ignition delay time for different biomass samples. At higher temperatures, the ignition delay time of different biomasses were relatively insensitive to temperature and converged to a similar value. These studies show that the sensitivity of combustion properties to co-flow temperature, composition, and flow rate is not linear, displaying a regime-dependent behavior.

In the fuel science literature, myriad TGA studies probe the influence of the biomass type [37,38], oxidizing environment composition [9,39,40], and heating rate [41] on thermal behavior of biomass. TGA heating rates (< 100 K/min) are orders of magnitude smaller than an industrial combustor (~10,000 K/sec), which raises doubt over whether TGA results can be linked to true combustion characteristics [10]. TGA and combustion experiments are rarely paired in the literature. Magalhaes et al. [42] conducted single-particle biomass combustion experiments in parallel with TGA, the results of which were used to assess the self-ignition risk of biomass during storage and transportation. Volatile ignition temperature and particle ignition temperature were obtained using a heating rate of 20 K/min using TGA, while ignition delay time and ignition mode data were obtained by burning the particles in an entrained flow reactor (EFR) under higher heating rates (~10^5 K/s) to resemble ignition under realistic heating conditions. The ignition temperatures obtained from TGA were 200-300 K lower than those measured in the EFR as the ignition criteria are different in these two types of experiments. Magalhaes et al. attribute the difference in ignition temperatures to the TGA study being kinetically controlled, while in combustion the reaction is O_2-diffusion controlled. Li et al. [43] studied the ignition behavior of woody biomasses in a down-fire furnace and analyzed the results alongside TGA data. Although TGA data showed that the presence of O_2 hastens the devolatilization process, it could not reveal the impact of particle size

on biomass ignition behavior as a result of the low heating rate and lack of motion of particles in the TGA. However, it is difficult to determine whether this behavior was due to enhanced devolatilization or how the ignition processes of the volatiles and char surface changed in the presence of air versus N_2.

Even though biomass combustion chemistry is generally governed by that of cellulose, a primary constituent of lignocellulosic biomasses [44,45], there are relatively few examples of cellulose combustion experiments in the literature. Wang et al. [28] studied the effect of cellulose, hemicellulose, and lignin on the ignition behavior of biomass in a drop tube furnace in an air atmosphere (heating rate of 10^4 K/s and furnace temperature of 1273 K) coupled with flame visualization. The dimmest light was detected at the time of cellulose ignition with a hetero-homogeneous ignition mode. The measured ignition delay time and burnout time of cellulose were 1 ms and 4 ms, respectively. The devolatilization rate of cellulose was faster than other lignocellulosic components. The authors concluded that the volatile cloud around the particle is mainly caused by the decomposition of cellulose and, regardless of the burning mode, the ignition temperature of biomass is close to that of cellulose. Unlike studies of cellulose combustion, TGA-based oxidation (and pyrolysis) experiments of cellulose are plentiful [37,46,47]. At typical TGA heating rates, cellulose starts to decompose around 598 K and loses over 80% of its initial mass before 683 K [37]. This indicates that cellulose ignitability depends on the initial pyrolysis step occurring around 593-643 K [47]. While lignocellulosic biomasses vary in composition anywhere from 25 – 50 wt% cellulose, 12 – 50 % hemicellulose, and 6 – 35 % lignin [48], this prior work in the field suggests that cellulose drives the oxidation and combustion properties of the biomass as a fuel.

It is unclear the extent to which rapid diagnostics used in the fuel science literature (e.g. TGA) can be used to predict the actual combustion behavior of biomass. To begin tackling this question, the present work probes the combustion characteristics of microcrystalline cellulose in a Hencken burner over a range of operating conditions to characterize several key combustion properties, notably ignition delay time and burnout time. These results are examined alongside TGA experiments and analyses routinely carried out in the fuel science literature. Cellulose is used extensively in the fuel science field as a model component to unravel the complex chemistry behind lignocellulosic biomasses [49]. As such, in this work microcrystalline cellulose (refined wood pulp) is chosen as the model biomass compound to validate and quantify the uncertainty of

combustion studies and provide a basis for aligning data from the combustion and fuel science communities. Companion scaling analyses together with the combustion and TGA data provide insight into the rate-controlling processes in cellulose combustion as well as their dependence on temperature and oxygen mole fraction of the oxidizing atmosphere.

2 Materials and Methods

2.1 Materials

Cellulose is often used as a model biomass compound given its homogeneity and prevalence in biomass [50]. Microcrystalline cellulose ($C_{12}H_{22}O_{11}$) supplied from Alfa Aesar (A17730) was investigated in this study. As determined using TGA (details available in the supplementary material), cellulose comprises 0.2 ± 0.3 wt% ash, 92.9 ± 0.6 wt% volatile matter, and 6.9 ± 0.4 wt% fixed carbon. Particle size separation was performed by means of dry sieving the particles; particles with a diameter of 25-37 μm were selected for testing. The sieving process was performed two times to minimize the uncertainty from particle size differences. Particle sizes were measured using a Microtrac particle size analyzer, as shown in Figure 1.

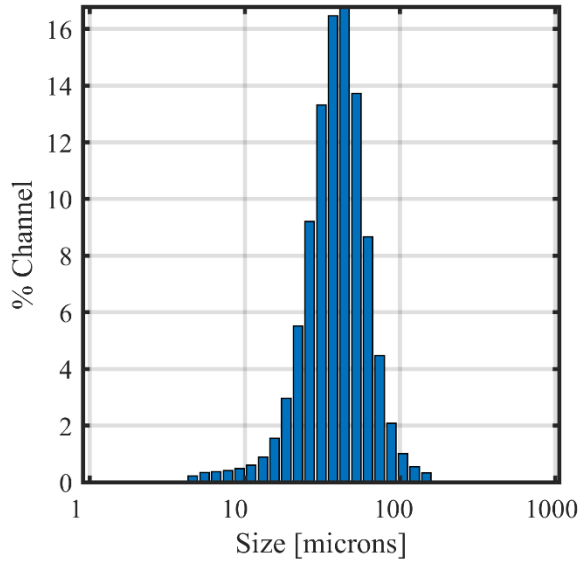

Figure 1. Particle size distribution of mechanically sieved microcrystalline cellulose.

2.2 Experimental methods

2.2.1 Combustion apparatus

The experimental setup used in this work consists of a Hencken burner, a fluidized bed, and the flow measurement system, as illustrated in Figure 2. The burner is fed by bottled oxidizer and fuel gases. Several oxidizers are used in this study, including air and various mixtures of oxygen and nitrogen. Hydrogen serves as the fuel for the co-flow stream in order to eliminate carbon in the hot gas products, allowing carbon-based imaging sources like CH* chemiluminescence to be used to visualize the cellulose particles' behavior only. The Hencken burner is a multi-diffusion flat flame burner that creates a post-combustion zone to ignite the solid fuel particles. The test section is a 35.56 mm diameter and 35.56 cm long quartz tube, which allows for optical access and prevents entrainment of outside air to the flame and particle stream. Using a fluidized bed seeder, the solid fuel particles are entrained by a pressurized carrier gas (N_2) flowing through the central port in the bottom of the burner. A DC vibration motor (Uxcell, 44×24mm, 12 V, 8000 RPM) is mounted to the bottom plate of the fluidized bed to insure fluidization.

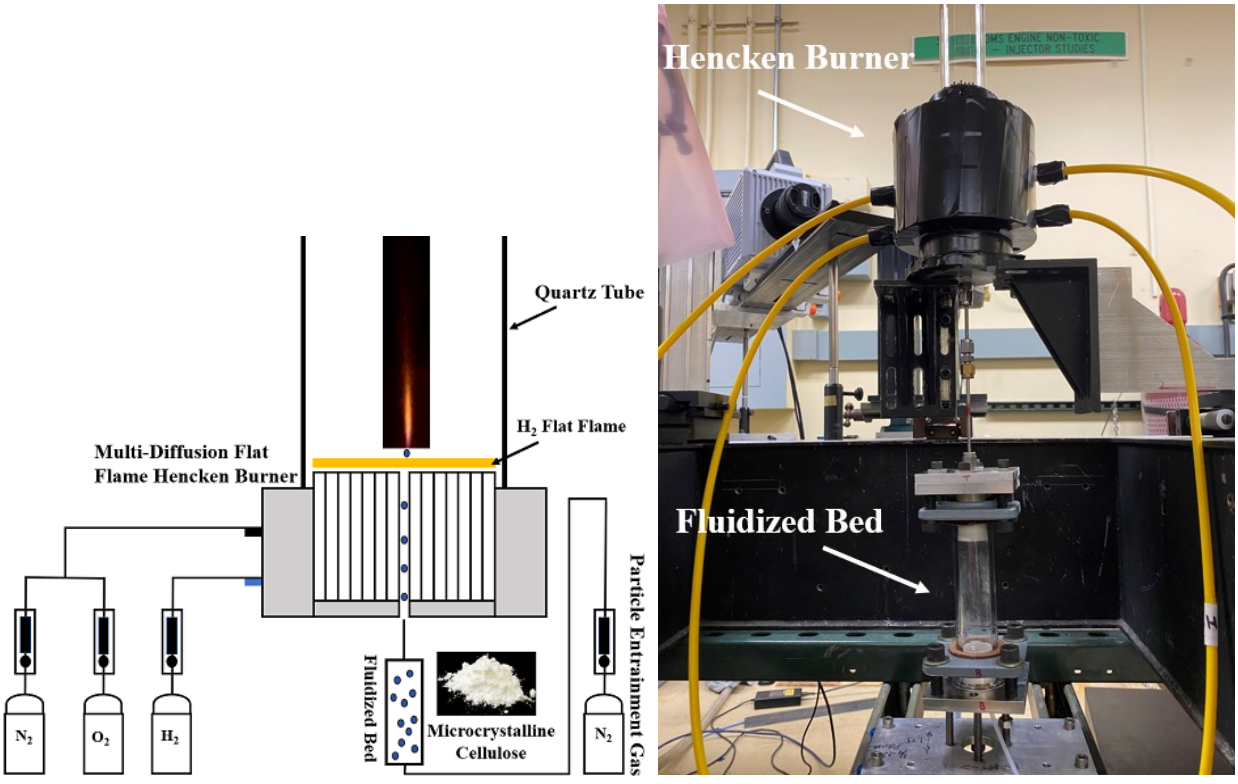

(a) (b)

Figure 2. (a) Schematic of the experimental rig and flow diagram, (b) image of the burner and fluidized bed

2.2.2 *Diagnostics*

Two diagnostics were simultaneously used to quantify the ignition delay time and volatile burnout time of the cellulose particles: chemiluminescence imaging and high-speed particle image velocimetry (PIV). An overhead schematic of the diagnostics is shown in Figure 3.

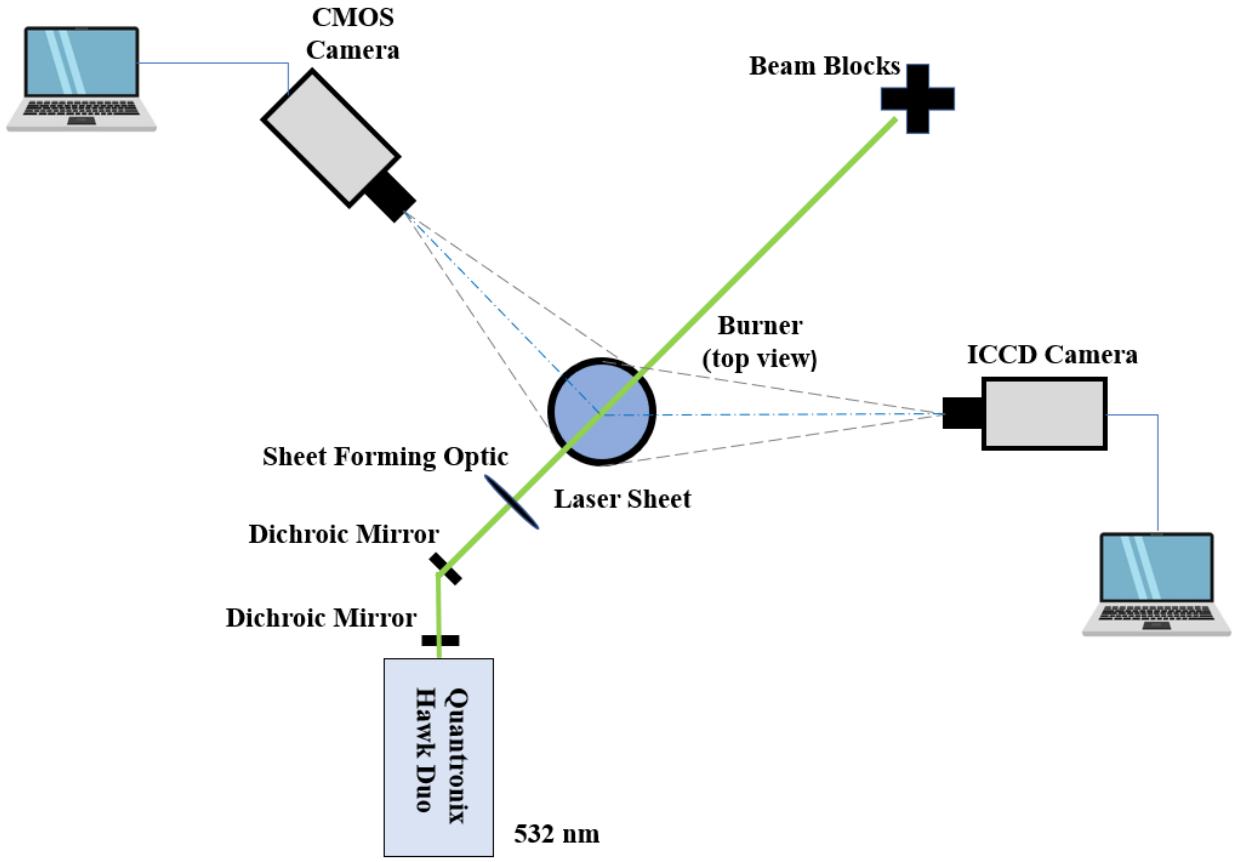

Figure 3. Schematic of the simultaneous CH* chemiluminescence, PIV, and two-color pyrometry diagnostics

CH* chemiluminescence imaging was performed to identify the different stages of particle combustion, from ignition to burnout. CH* chemiluminescence was imaged using a PI-MAX (Gen II) intensified camera with a 50 mm f /1.4 lens (Nikon AF NIKKOR), filtered using a 430 nm bandpass optical filter (Andover Corporation, FWHM +/- 10 nm). The gain and exposure time were set based on the brightness of signal at each operating condition to avoid saturated pixels while obtaining sufficient signal and a signal to noise ratio greater than 8; the resulting images are corrected so they can be compared on the same colorscale. A total of 100 filtered images are captured for each dataset with total image sampling duration of ~ 2.5 minutes.

High-speed particle image velocimetry was used to measure the velocity of the cellulose particles. This velocity is used in conjunction with the CH* chemiluminescence images to calculate key combustion timescales. A dual-cavity, diode-pumped, solid-state laser, Nd:YAG laser (Quantronix Hawk Duo-532-60-M/Rev.A) operating at 532 nm is used for PIV. A high-speed CMOS sensor camera (Photron FASTCAM SA1.1) equipped with a 60 mm f/2.8 lens (Nikon AF Macro Nikkor) is used with a laser-line filter in front to reduce flame luminosity. The laser passes through a LaVision sheet-forming optic with a focal length of f=-10 mm, creating a laser sheet that is aligned with the central tube of the burner. The camera is positioned perpendicular to the laser sheet and the macro lens is used to provide a narrow field of view and a higher magnification of the jet of particles. The PIV domain size is 120 mm in the streamwise direction and 36 mm in the cross-stream direction. Laser-illuminated images are collected at 2.5 kHz acquisition rate in double frame mode, with a laser pulse time separation of 35 μs and 1024×1024 pixel resolution. LaVision DaVis 8.3 multi-pass cross-correlation algorithm is used for the velocity calculation from the collected images. Velocity vectors are computed using a multi-pass algorithm with interrogation window sizes ranging from 64x64 to 16x16 pixels and with 50% overlap for each pass, resulting in a vector spacing of 1.17 mm/vector. A total of 5000 vector fields are obtained for each condition. The uncertainty of the time-averaged velocity from DaVis 8.3 cross-correlation algorithm is 0.005-0.11 m/s in the jet core.

2.2.3 Data Analysis

The first 23.4 cm of the burner were imaged to capture the entire luminous flame zone across all operating conditions. 100 images were obtained for each condition and several test conditions were repeated at least three times to gauge repeatability. Examples of the raw images' individual centerline profiles are provided in the supplementary material. Figure 4a shows an example of the time-averaged centerline intensity profile analysis that is used to determine the ignition delay time and volatile burnout time. The combustion zone is bounded by the ignition location, x_1, and volatile burning end location, x_2. The ignition location, x_1, is defined as the location where the centerline intensity profile reaches 50% of its maximum value. Comparison of this ignition delay definition to one based on a maximum gradient method is provided in the supplementary material; both methods resulted in the same trends and, for many conditions, the same ignition delay times within the range of uncertainty. The volatile burning distance, (x_2- x_1), is defined by the full-width-half-

max (FWHM) of the centerline intensity curve. These length scales can be converted into the corresponding time scales – the ignition delay time, τ_{ig}, and volatile burning time, τ_b – using the jet particle velocity.

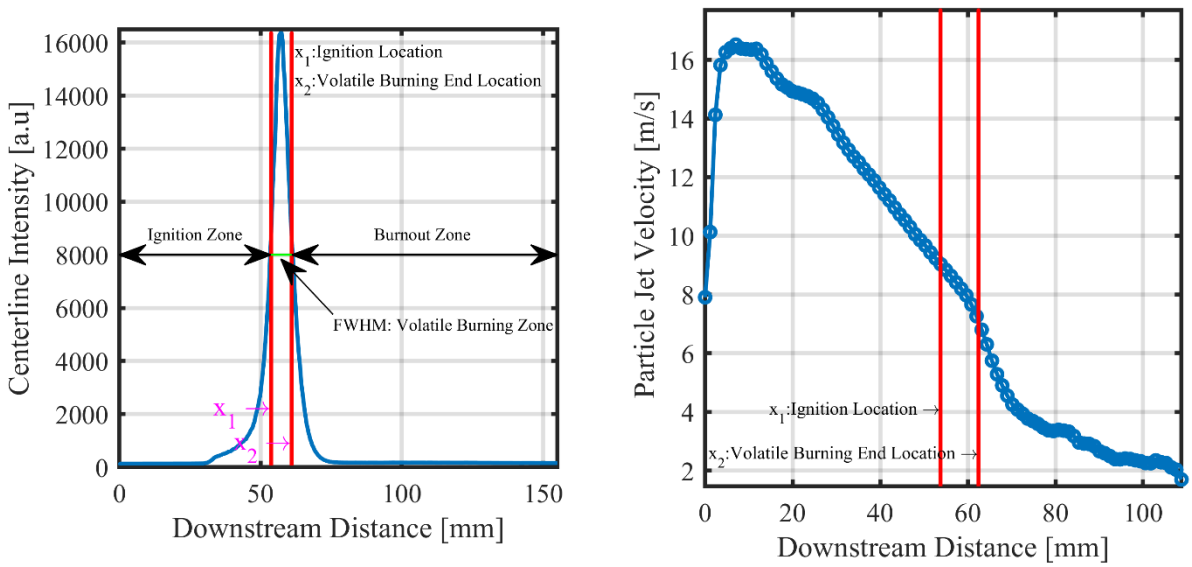

(a) **(b)**

Figure 4. Example of (a) intensity analysis a time-averaged CH* chemiluminescence image of cellulose particles and (b) superimposition of length scales obtained from CH* chemiluminescence imaging on particle jet velocity profile.

The ignition delay time, τ_{ig}, and the volatile burnout time, τ_b, are calculated using the time-averaged centerline intensity profile from the CH* chemiluminescence images and the time-averaged centerline velocity data from PIV, which were measured simultaneously. The time scales τ_{ig} and τ_b are defined in Eqs (1-2):

$$\tau_{ig} = \sum_{i=1}^{i=x_1} \frac{x_{i+1} - x_i}{u_i} \qquad (1)$$

$$\tau_b = \sum_{i=x_1}^{i=x_2} \frac{x_{i+1} - x_i}{u_i} \qquad (2)$$

Where x_i and u_i are the corresponding position and particle velocity in the discretized region along the streamwise direction. Figure 4b shows an example centerline velocity profile with the ignition location and burn-out zone indicated in vertical red lines. In this velocity profile, the particles begin at a high velocity as they exit the small tube from the fluidizer to the test section.

As the particle jet entrains surrounding low-momentum gas, the velocity of the particles decreases significantly. Most particles are burnt by the end of the volatile burning location and so velocity data downstream of this location is not highly reliable and is not used in any calculations.

2.2.4 Uncertainty analysis

A multivariate uncertainty analysis approach is used to quantify the uncertainty of combustion time scales τ_{ig} and τ_b. In this formulation, $\tau = f(x, u)$. Thus, uncertainty propagates due to the experiment errors and statistical variations in locating the ignition location, x_1 , the volatile burning end location, x_2, and the particle velocity, u. This section describes the uncertainty analysis; details on the statistical repeatability study are discussed in the supplemental material.

The uncertainty in τ_{ig}, as a function of x_1 and u, is denoted by $d\tau_{ig}$:

$$d\tau_{ig} = \sqrt{\left(\frac{\partial \tau_{ig}}{\partial x_1} dx_1\right)^2 + \left(\frac{\partial \tau_{ig}}{\partial u} du\right)^2} \tag{3}$$

For a given operating condition in the test matrix, the first term on the right-hand side (RHS) includes the sensitivity of τ_{ig} with respect to the variation of x_1 in each CH* imaging data set multiplied by dx_1, the inner quartile range (IQR) of the x_1 population. To calculate the first term, the time-averaged local particle jet velocity is assumed to be the median value of all time-averaged velocity measurements for a given operating condition. For example, one dataset includes 600 samples of x_1 obtained from six repeated experiments of 100 CH* images at each condition, excluding the outliers. Outliers are defined as points that are outside 1.5 times the IQR of a dataset. Using these data, τ_{ig} is calculated for every individual x_1 , and $\frac{\partial \tau_{ig}}{\partial x_1}$ is calculated using the slope of the regression line derived from a $\tau_{ig} - x_1$ scatterplot. The second term on the RHS refers to the variation in τ_{ig} with respect to the change in u. Likewise, having the local particle jet velocity dataset for each velocity measurement at a given operating condition and considering the median value of the x_1 population, τ_{ig} is computed for every individual u dataset. The sensitivity, $\frac{\partial \tau_{ig}}{\partial u}$, is calculated using the slope of the regression line obtained from the $\tau_{ig} - u$ scatter plot, where u_i is a representative local velocity at the closest point to x_1 and du is the IQR of u_i. The same

procedure is implemented to calculate $d\tau_b$, however, τ_b is a function of three variables of x_1, x_2 and u, as shown in Equation 4.

$$d\tau_b = \sqrt{\left(\frac{\partial \tau_b}{\partial x_1} dx_1\right)^2 + \left(\frac{\partial \tau_b}{\partial x_2} dx_2\right)^2 + \left(\frac{\partial \tau_b}{\partial u} du\right)^2} \quad (4)$$

In cases where repeated data sets are not available for every operating condition, the sensitivity of the timescales to uncertainty in the ignition and burnout locations as well as the velocity data is calculated in a slightly different manner. To calculate $\frac{\partial \tau}{\partial u}$, a subset of 100 out of 5000 PIV image frames is randomly selected, the centerline particle jet velocity is calculated, and $\frac{\partial \tau}{\partial u}$ is determined from the slope of the regression line fitted for the scattered $\tau - u$ plot, where u_i is a representative local velocity at the closest point to x_1 and du is the uncertainty of the time-averaged velocity vector field at the corresponding location. In this case, the *du* term in the equation is taken from the uncertainty of the vector calculation in DaVis, rather than from a statistical analysis of multiple experiments. In this way, the uncertainty is quantified from within one dataset rather than multiple datasets, as repetition of each operation condition several times was not tractable in a test matrix as large as the one in this study.

It is expected that the largest source of variability, and hence uncertainty, in the reported values is a result of variations in particle fluidization; every other operating parameter was highly controllable. To this end, great care was taken to ensure that preparation of the fluidized bed was standardized and fluidization remained consistent between experiments.

2.2.5 Thermogravimetric analysis

TGA was performed using a TA Instruments SDT 5500 Thermogravimetric Analyzer. For proximate analysis, ~5 mg cellulose was loaded on a platinum crucible. N_2 flowed through the instrument at 25 mL/min. The temperature ramped from ambient to 383 K at 10 K/min, where it remained for 30 min; the mass loss in this segment was attributed to moisture. The temperature was then raised at a rate of 10 K/min to 1173 K, followed by another 30 min hold; the mass loss in this segment was attributed to volatile matter. The gas flow then switched from N_2 to air and the temperature ramped at 10 K/min to 1223 K and held for a final 30 minutes; the mass loss in this segment is attributed to fixed carbon. The residual mass is generally considered to be ash. To

perform oxidation studies, ~5 mg cellulose was loaded on a platinum crucible, the temperature was raised to 383 K, held for 30 min to remove moisture, and then the temperature was raised to 1123 K at a constant heating rate (5, 10, 25, 50, 100 K/min) in 25 mL/min air. Data are taken every 0.6 seconds. To reduce noise, each TGA curve was smoothed by applying a first-order Savitzky-Golay filter with a window of 101 points. For both proximate and oxidation analyses, all conditions were triplicated and an average and standard deviation for replicates (along the temporal axis) below 0.5 % was considered acceptable. Derivative TGA ($DTG = dw/dt$ [wt%/min]) curves were calculated by differentiating the TGA curves along the temporal axis to highlight devolatilization trends.

Three temperatures were determined from the DTG curves: T_i, ignition temperature where weight loss increases to 1%; T_p peak temperature where weight loss rate is maximum; and T_b, burnout temperature where the weight loss decreases to 1%. A common approach in the fuel science literature is to assess the combustion performance of a solid biofuel using DTG data to calculate a combustibility index, S (Eq. 5, where dw/dt is the mass loss rate and T_i and T_b are in °C). S is often used as a comprehensive representation of the ignitability, (so-called) combustion rate, and burnout of the fuel. The literature assumes that quicker and earlier ignition and faster burnout (defined as $S > 2 \cdot 10^{-7}$) describe better fuels [51–53]. Interestingly, following multiple citation chains reveals scant real evidence to support these findings [54–56] or leads to studies that cannot be found in the literature (e.g., [57]). However, given prevalence of this parameter across the fuel science literature, we include the S parameter in our investigation to assess its viability as a combustion indicator for biomass.

$$S = \frac{\left(\frac{dw}{dt}\right)_{max} * \left(\frac{dw}{dt}\right)_{mean}}{T_i^2 * T_b} \quad (5)$$

3 Combustion of Cellulose in Air

The first experiment varied the equivalence ratio of the H_2/air flame; the parameters were defined by operability studies varying H_2/air (0.2-1 in steps of 0.05) using one particle flow rate to determine the quality and stability of the H_2 flame in the Hencken burner. The test matrix, shown in Table 2, represents the conditions where the Hencken burner flame was stable and flat; lower equivalence ratios resulted in unstable flames and higher equivalence ratios resulted in very tall flames that interfered with the ignition imaging region of the cellulose. During this test, we ensured

that the central N_2 jet for particle transport did not change the flame structure or operability limit. Based on the results of the operability testing, the final test matrix includes five equivalence ratios for the H_2/air flames. The entrainment gas flow rate is maintained at 0.38 slpm, which is the minimum flow rate necessary to provide continuous particle fluidization. The adiabatic flame temperature, T_{ad}, and product oxygen concentration of the co-flow H_2 flames in the Hencken burner were calculated using GRIMech 3.0 [58] and the equilibrium solver in Chemkin [59]; results are shown in Table 1. As the equivalence ratio, ϕ, increases, the surrounding gas temperature increases, which would tend to reduce ignition delay and burnout times. However, as ϕ increases, the oxygen concentration decreases, which should have the opposite effect. The results in this initial study show the compounding effects of varying temperature and oxygen concentration and capture the impacts of burning biomass in a co-fired configuration.

Table 1. Test matrix of cellulose combustion in air atmosphere.

ϕ	Air (slpm)	H_2 (slpm)	T_{ad} (K)	O_2 mole fraction in combustion products
0.3	18.16	2.32	1186	0.13
0.35	18.16	2.71	1308	0.12
0.4	18.16	3.1	1424	0.11
0.45	18.16	3.48	1535	0.10
0.5	18.16	3.87	1640	0.09

3.1 Ignition delay time and volatile burning time

The ignition delay and volatile burning times derived from the CH* chemiluminescence imaging and velocity data are shown in Figure 5; time-averaged chemiluminescence images are provided in the supplemental material. Results show that increasing the equivalence ratio, accompanied by increasing T_{ad}, results in a shorter ignition delay time, from 5.2 $msec$ at ϕ = 0.35 to 2.7 $msec$ at ϕ = 0.5. The uncertainty in the ignition delay time is relatively constant across all operating conditions. The normalized sensitivity of T_{ad} to equivalence ratio over this range of equivalence ratios is 0.63, whereas the normalized sensitivity of the O_2 product mole fraction is -0.75, on the same order as the sensitivity to T_{ad}. The fact that that ignition delay decreases with increasing equivalence ratio suggests that ignition delay time is a stronger function of temperature than O_2 concentration, as the ignition timescales decrease with increasing temperature but

decreasing oxygen concentration. The volatile burning time is independent of the equivalence ratio of the flat flame over most equivalence ratios within the bounds of uncertainty, although the uncertainty of the volatile burning time is slightly higher for ϕ = 0.35 as compared to the other conditions.

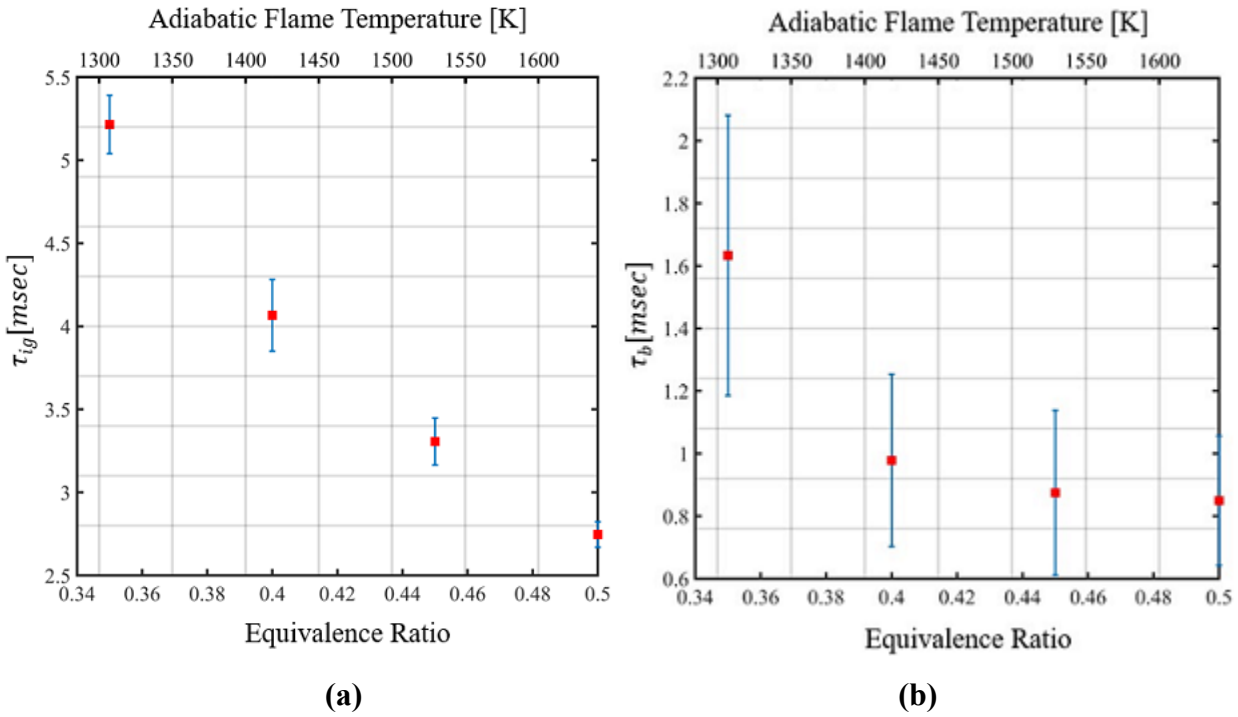

(a) **(b)**

Figure 5. (a) Ignition delay time and (b) volatile burning time of microcrystalline cellulose particles vs. H_2/air flame equivalence ratio.

4 Combustion of Cellulose in O_2/N_2

The previous results of cellulose combustion in air suggested that the temperature effect on ignition delay time was stronger than the oxygen mole fraction effect. In these experiments, the temperature and oxygen mole fraction effects on the combustion behavior of particles are controlled separately using binary mixtures of O_2/N_2 with various equivalence ratios to directly measure the sensitivities. Table 2 presents the test matrix designed for combustion of cellulose particles with varying concentrations of O_2 and N_2 in the oxidizer. In the first set of cases, the equivalence ratios are chosen such that T_{ad} is constant for each individual O_2/N_2 mixture. For the second set of cases, equivalence ratios are chosen such that O_2 mole fraction in the surrounding combustion products is constant for each O_2/N_2 mixture.

Table 2. Test matrix of cellulose combustion in O_2/N_2 atmosphere.

Constant adiabatic flame temperature, varying O_2 concentration in H_2 combustion products			
O_2 (%) in the reactant mixture	**ϕ**	**$T_{ad}\ (K)$**	**O_2 mole fraction in combustion products**
12.0	0.87	1645	0.01
13.5	0.77	1645	0.02
15.0	0.70	1645	0.04
16.5	0.63	1645	0.05
18.0	0.58	1645	0.06
21.0	0.50	1645	0.09
25.0	0.42	1645	0.12
30.0	0.35	1645	0.17
Constant O_2 concentration in combustion products while varying H_2 adiabatic flame temperature			
O_2 (%) in the reactant mixture	**ϕ**	**$T_{ad}\ (K)$**	**O_2 mole fraction in combustion products**
15.0	0.50	1329	0.06
16.0	0.52	1430	0.06
17.0	0.54	1527	0.06
18.0	0.56	1618	0.06
19.0	0.58	1706	0.06

4.1 Key combustion time scale

Figure 6 shows the variation in the centerline time-averaged CH* chemiluminescence profiles with variation in product oxygen mole fraction; the time-averaged images are provided in the supplementary material. The combustion behavior changes dramatically as the oxygen concentration varies, where the trend is divided into two regimes: one with a product oxygen mole fraction of 0.01 to 0.05 and one with a product oxygen mole fraction of 0.06 to 0.17. In the low-oxygen regime, the particle flames are very long and the chemiluminescence signal is very low, indicating weak burning and slow burnout times. In the high-oxygen regime, the particle flames are shorter and much more intense. In this regime, increasing the oxygen mole fraction increases

the intensity of the flame, likely the result of higher heat release from more available oxygen, but the ignition location does not change significantly.

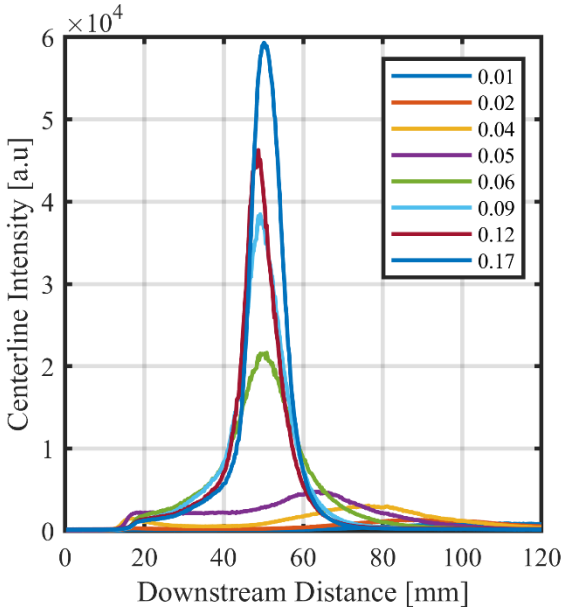

Figure 6. Centerline CH* chemiluminescence intensity profiles with different O_2 mole fraction with constant T_{ad}.

The centerline profiles show a general decreasing trend in both ignition location and the duration of the combustion as the O_2 concentration increases, indicating more rapid combustion processes overall. The ignition process depends on the devolatilization rate as well as the local reactivity of the mixture. The devolatilization process is highly sensitive to temperature and, as such, is expected to be constant for all O_2 mole fractions at a given T_{ad}. However, ignition delay is dependent on the oxygen concentration; a higher O_2 concentration results in a shorter ignition delay. The influence of O_2 concentration on ignition location in cases with lower O_2 concentration is stronger than that with higher O_2 concentration. At O_2 product mole fractions above 0.06, there is little variation in the ignition location. Similarly, peak location is dependent on both the ignition process as well as the rapidity of the volatile burning process. FWHM, which indicates the duration of volatile matter combustion, also decreases by increasing the O_2 mole fraction. As the O_2 product mole fraction increases, the gaseous volatiles react more quickly as the concentration of diluents is lower. These lower-diluent reactions also release more heat, which in turn enhances reaction rates by increasing the local temperature. Although the devolatilization process is an endothermic process and likely occurs during volatile burning, the intensity of the volatile burning at higher O_2

mole fractions is dominant as compared to the absorbed heat by devolatilization. The results of the volatile burning end location track that of the ignition location and FWHM.

Figure 7 shows a series of centerline intensity profiles of the time-averaged CH* images as a function of downstream distance at a constant co-flow oxygen mole fraction of 0.06 and variation in adiabatic flame temperature of the hydrogen flame. The time-averaged images are provided in the supplemental material. As the co-flow temperature increases, the ignition location moves further upstream, likely a result of the faster ignition kinetics of the volatile gases. Additionally, higher temperatures result in more intense burning, as indicated by the intensity of the CH* signal. Over the selected temperature range, increasing temperature decreases ignition location, peak location, and volatile burning end location, resulting in accelerated ignition processes. However, the FWHM is not notably affected by the surrounding hot temperature despite changes in the adiabatic flame temperature from 1329K – 1706 K over this operating range.

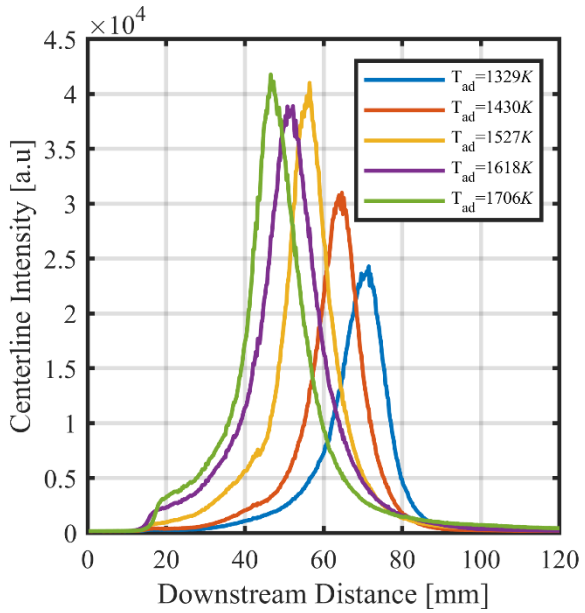

Figure 7. Time-averaged centerline intensity profile at different O_2 concentrations under O_2/N_2 environment while O_2 concentration in combustion product is constant.

The characteristic ignition delay time and volatile burnout times of the cellulose are calculated using the length scales from the CH* imaging (provided in the Supplementary Material) and the time-averaged axial velocity profiles from PIV. Results are presented in Figure 8 and Figure 9 for cases of constant flame temperature and constant co-flow O_2 mole fraction, respectively.

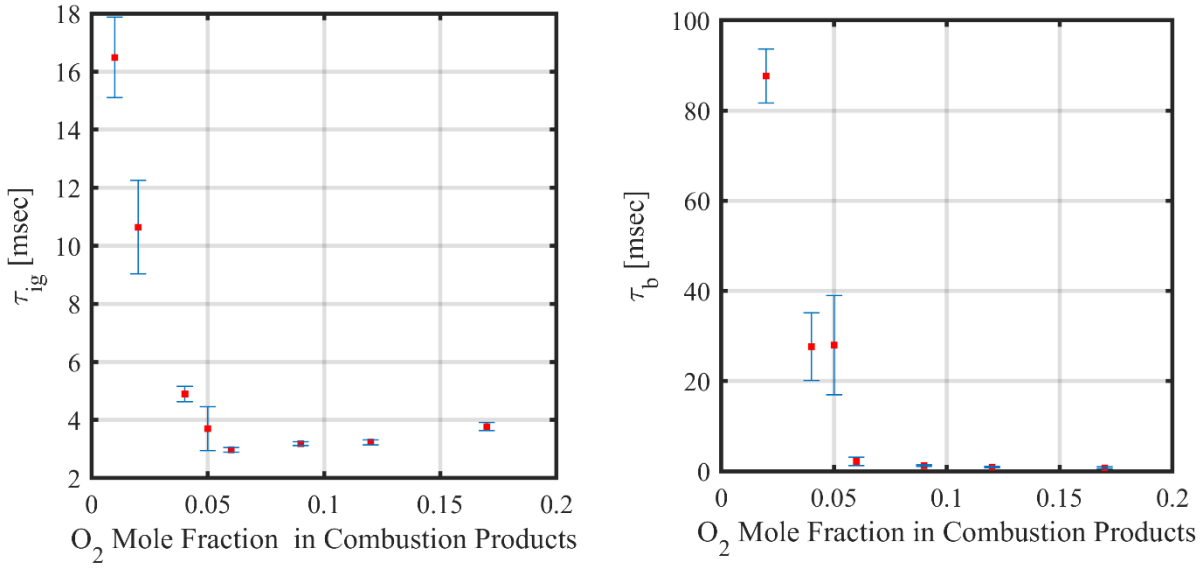

(a) **(b)**

Figure 8. (a) Ignition delay time and (b) volatile burning time of microcrystalline cellulose particles vs. O_2 product mole fractions while T_{ad} is constant.

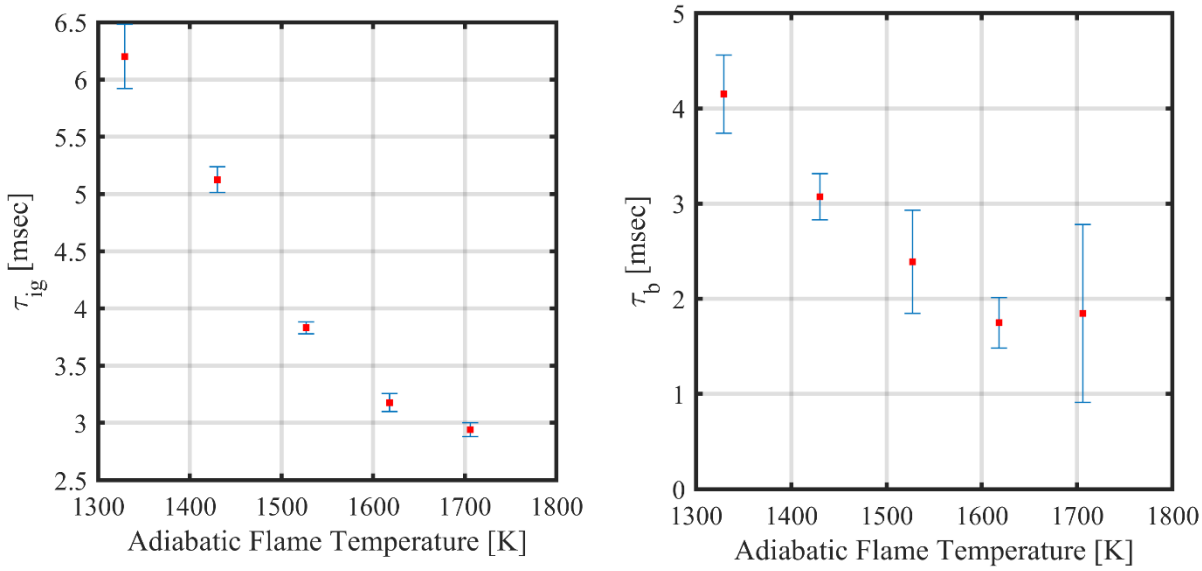

(a) **(b)**

Figure 9. (a) Ignition delay time and (b) volatile burning time of microcrystalline cellulose particles vs. temperature while O_2 mole fraction in combustion products is constant.

At the constant-temperature conditions, there are two regimes of ignition delay time as the product oxygen mole fraction varies: one in the range of 0.01-0.05 and one in the range of 0.06-

0.17. At the low O_2 conditions (0.01-0.05), ignition delay time is highly sensitive to product O_2 mole fraction, with a dramatic decrease in ignition delay time with increase in O_2. At higher O_2 mole fractions, the ignition delay time is not as sensitive to O_2 mole fraction. The same trends hold for the volatile burnout time. Ignition delay time and volatile burnout time are monotonically dependent on surrounding temperature at a constant O_2 mole fraction, as shown in Figure 9, where increasing temperature decreases both timescales. Higher uncertainty in the case of O_2 mole fraction of 0.05 was caused by the higher fluctuations at the regime transition.

One of the key research questions this paper pursued is whether cellulose combustion timescales are more sensitive to surrounding oxygen mole fraction or surrounding temperature. To answer this question, a normalized sensitivity for both timescales has been calculated for three trends: variation in timescale vs. O_2 mole fraction for low O_2 levels, variation in timescale vs. O_2 mole fraction for high O_2 levels, and variation in timescale vs. temperature. In this calculation, the timescales are normalized by their mean value over the range of values considered. The oxygen mole fractions and temperatures are similarly normalized by the mean value over the ranges considered: 0.03 O_2 for the 0.01-0.05 range, 0.115 O_2 for the 0.06-0.17 O_2 range, and 1518 K for the variation in temperature.

Table 3 shows the sensitivity of both ignition delay time and volatile burnout time to product O_2 mole fraction. Similarly, Table 4 shows the sensitivity of the ignition delay time and volatile burnout time to surrounding temperature. Interpretation of these sensitivities requires consideration of how the oxygen content and temperature of the surrounding gases control the rate-limiting processes that, in turn, control the ignition delay time and volatile burnout time. Ignition delay time in the experiment is a measure of both the devolatilization process as well as the chemical ignition process. Both processes are highly sensitive to surrounding gas temperatures, where increasing temperature decreases the timescale of both processes. However, the devolatilization process is not a function of the surrounding O_2 mole fraction, whereas O_2 mole fraction can moderate ignition chemistry. Similar considerations should be made for the volatile burnout time. During this time, some devolatilization is likely occurring, although the most dominant process is likely combustion of the volatile gases. The temperature that controls both the devolatilization process as well as the kinetic rates is then the flame temperature of the volatiles, rather than the surrounding gas temperature. This flame temperature is not measured in this study

but increases with increasing surrounding gas temperature based on thermochemical equilibrium considerations.

Given these factors, we can interpret the sensitivities of the ignition delay time and volatile burnout time to both surrounding gas oxygen mole fraction and temperature. In all but one case, the sensitivities are negative, which means that increases in O_2 mole fraction and temperature result in shorter timescales. The sensitivity of both timescales to temperature is almost three times stronger than the sensitivity to oxygen mole fraction in the low-O_2 region, where the reaction is generally starved of oxygen. This greater sensitivity to temperature as compared to O_2 mole fraction is likely a result of the dependence of both devolatilization and chemical rates on temperature. Increasing the temperature hastens two rate-limiting processes, whereas increasing the O_2 mole fraction only quickens one.

Table 3. Sensitivity of combustion timescales to O_2 mole fraction in the combustion products with constant T_{ad} = 1645 K.

	Sensitivity	
	$\frac{\partial(\frac{\tau_{ig}}{\overline{\tau_{ig}}})}{\partial(O_2/\overline{O_2})}$	$\frac{\partial(\frac{\tau_b}{\overline{\tau_b}})}{\partial(O_2/\overline{O_2})}$
O_2 (0.01 – 0.05)	-1.1	-1.33
O_2 (0.06 – 0.17)	0.23	-1.02

Table 4. Sensitivity of combustion timescales to T_{ad} with product O_2 mole fraction of 0.06.

	Sensitivity	
	$\frac{\partial(\frac{\tau_{ig}}{\overline{\tau_{ig}}})}{\partial(T_{ad}/\overline{T_{ad}})}$	$\frac{\partial(\frac{\tau_b}{\overline{\tau_b}})}{\partial(T_{ad}/\overline{T_{ad}})}$
T_{ad} (1329 – 1706 K)	-3.23	-3.66

4.2 Thermogravimetric analysis

Details of proximate analysis (moisture, volatile matter, fixed carbon, and ash) conducted via TGA are available in the supplementary material. The proximate analysis confirms that over 99.7 wt% of the cellulose material is oxidizable matter with the vast majority (93 wt%) being volatile matter. Companion TGA and DTG curves for microcrystalline cellulose under inert nitrogen

(CLS-N2) and oxidative air atmospheres (CLS-Ox) are shown in Figure 10 as a function of TGA temperature (additional oxidation curves as a function of reaction time available in supplementary material). The oxidative experiments were performed at five heating rates, whereas the experiment in the inert environment was performed at a heating rate of 10 K/min only. The use of TGA oxidation data to represent combustion behavior is primarily criticized because of the slow heating rates experienced by samples, upon which reaction rates depend [60]. This limitation is highlighted in Figure 10; increasing the heating rate shifts mass loss to higher temperatures. At higher heating rates, the furnace temperature increases on a shorter timescale than the heat transfer to the sample for the same temperature increase. Since mass loss is controlled by the sample temperature and not that of the furnace, this behavior appears as a delay in the sample mass loss. The time required for mass loss is inversely proportional to reaction rate; complete oxidation occurs at higher temperatures for higher heating rates (Figure 10a) while the rate of decomposition is faster at higher heating rates (Figure 10 b). In both the time-based and temperature-based curves (see supplementary material), the decomposition occurs in two stages: a stage of very rapid mass loss where approximately 80% of the mass is lost for all cases, and then a slower mass loss regime where the remaining 20% of the mass decomposes.

Up to ~670 K, the effect of inert/oxidative atmosphere at the same heating rate of 10 K/min is minimal, as TG curves almost overlap. Above 670 K, the atmosphere plays a role in the mass loss of the small fraction of cellulose that was not decomposed at lower temperatures, suggesting that cellulose mass loss is driven by devolatilization rather than oxidation—this result is consistent with previous TG of cellulose [38,43]. In the air atmosphere, a second DTG peak appears between 725 and 850 K, indicating the oxidation of the cellulose fixed carbon fraction.

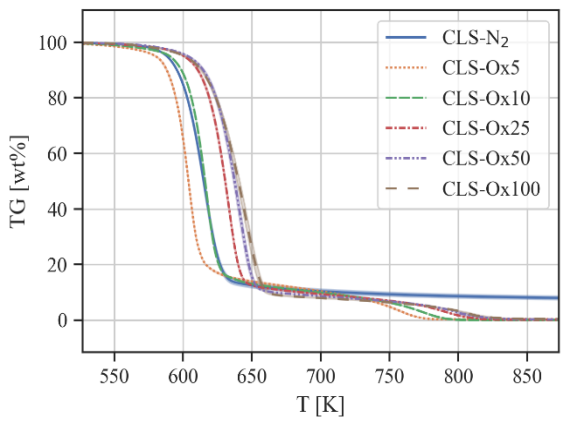

a)

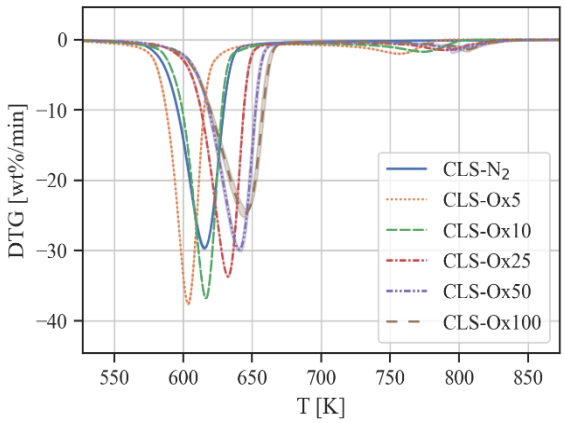

b)

Figure 10: TGA (a) and DTG (b) curves for cellulose in inert (CLS-N_2, heating rate of 10 K/min) and oxidative (CLS-Ox, followed by the heating rate) atmosphere. Central lines represent the average and shades represent the standard deviation of triplicates.

The effects of atmosphere and heating rate on T_i, T_p, T_b, and S are shown in Figure 11. For both T_i and T_p, which indicate the beginning (1% of mass loss) and the maximum rate of TGA devolatilization (peak DTG curve), there is almost no difference between the results in the inert and oxidative atmospheres. This result indicates that cellulose mass loss at these temperatures is not due to oxidation of volatile matter or char, but rather to devolatilization and pyrolysis. The peak mass loss rate temperature increases with heating rate. This is because devolatilization is occurring at a higher temperature with an excess of energy to overcome the initial activation energy and react at a faster rate [61]. This mirrors the finding in the burner study, namely that increasing temperature decreases the ignition timescale (peak DTG rate = maximum oxidation rate). This result does not hold for T_b, burnout temperature, which changes with atmosphere since it is directly dependent on the oxidation of fixed carbon (and therefore cannot take place without oxygen); it is only slightly influenced by the heating rate.

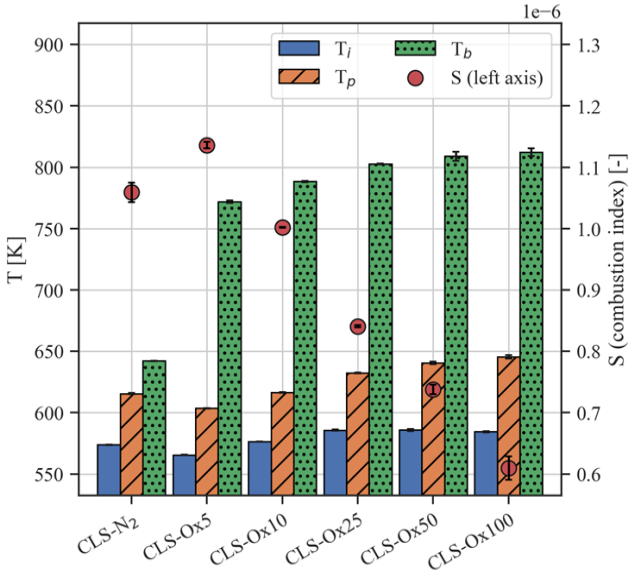

Figure 11. Combustion indicators (T_i, T_p, T_b, left axis and S, right axis) for cellulose in inert (CLS) and oxidative (CLS-Ox, followed by the heating rate) atmosphere. Error bars indicate one standard deviation of triplicate measurements.

However, though the T_p and T_i behavior mirror that of the burner studies, they are in no way predictive of actual combustion properties, and we caution our readers (and encourage further enquiry into this matter) about drawing significant conclusions from such TGA data. The burner studies indicate how the ignition timescales decrease with increasing temperature but decreasing oxygen concentration (Figure 8 and Figure 9). The TGA-measured ignition temperatures and burnout temperatures have a logarithmic dependence on heating rate (Figure 12a). Let us suppose that the heating rate in the burner-based combustion studies could be approximated (order of magnitude, that is!) by dividing the ignition delay time by the adiabatic flame temperature, putting heating rate on the order of magnitude of $2.5 \cdot 10^7$ to $4 \cdot 10^7$ K/min. As shown in Figure 12b, application of the log fit equation to heating rates of this level predict ignition temperatures of only ~ 655 K; half to one-third of what we measure in the Hencken burner. Given this, there is relatively little evidence that TGA-based T_i (or T_b, see Figure 14 c) would be a relevant predictor of any actual combustion behavior, though it may provide a reasonable basis of comparison among biomass-based fuels for utilization by slow oxidation.

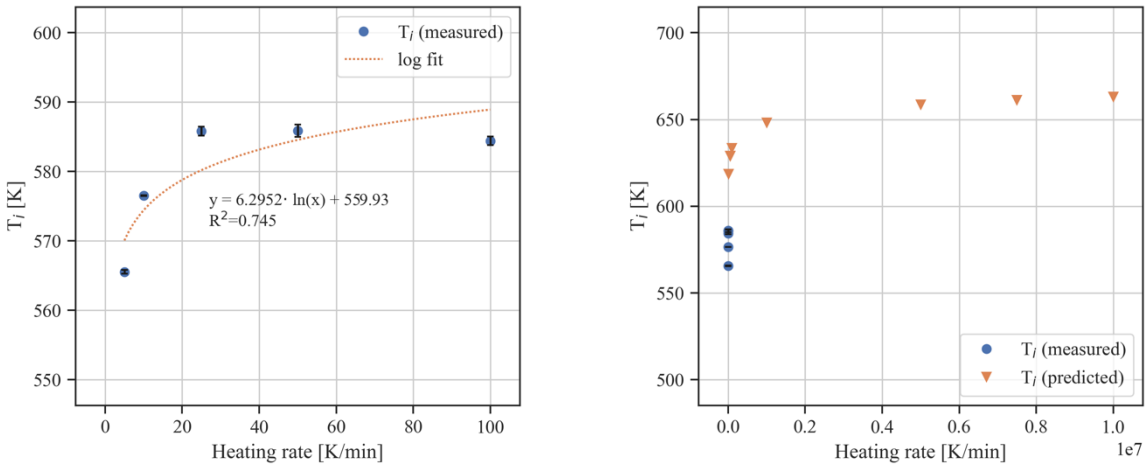

a) **b)**

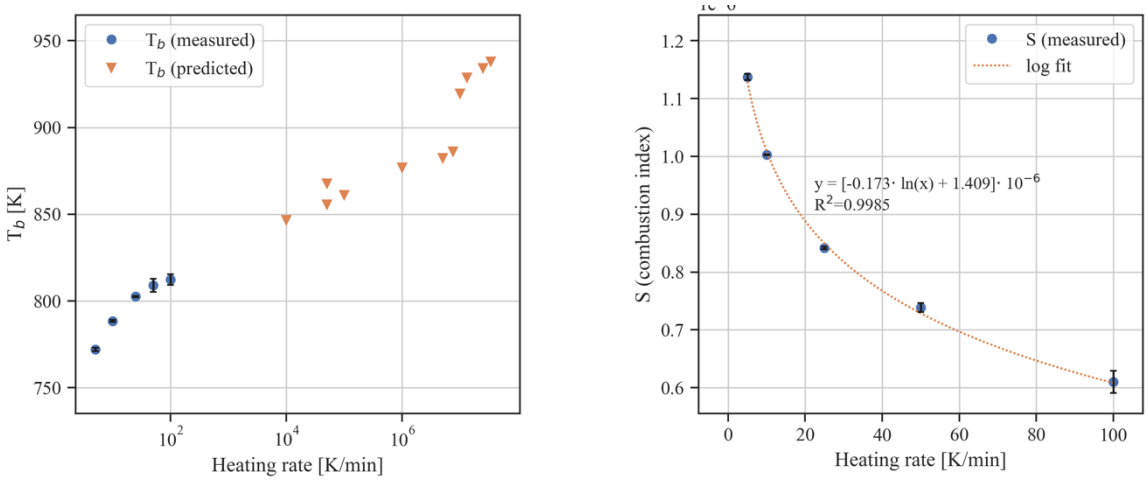

c) **d)**

Figure 12. Issues with projecting TGA-measured combustion indicators as shown through (a) logarithmic fit of T_i vs. heating rate (error bars indicate one standard deviation); (b) use of fitted equation to predict ignition temperature at combustion-relevant heating rates (c) log-linear plot of T_b vs. heating rate including predicted values from fitted equation; (d) logarithmic fit of S vs. heating rate (error bars indicate one standard deviation)

The variation in the S parameter with atmosphere and heating rate is small compared to typical variations among compositionally different samples (up to five-fold in Ref. [52]). This result is expected as the S parameter is intended to describe the intrinsic combustibility of the sample and not the effect of local atmospheric conditions. Interestingly, the difference in S between inert and oxidative atmospheres at the same heating rate is small compared to the difference across heating rates, which indicates that the devolatilization process is not driven by oxidation of volatiles, but mostly by pyrolysis. Cellulose has a higher S value ($6–11 \cdot 10^{-7}$) compared to solid fuels such as low-rank coal ($1.93 \cdot 10^{-7}$) [62]. We note that while fuels with a higher S values are often touted to exhibit "better combustion behavior" in the biofuel field, our results indicate that the S value alone should not be used in such a declarative manner. Rather, S is a single combustion parameter that may well describe the tendency of a fuel to volatilize without being able to distinguish between pyrolysis and oxidation regimes.

A further criticism of this S combustibility index arises when we look at these results alongside the Hencken burner studies. Given the extreme dependence of S on heating rate (Figure 12d) and the orders of magnitude slower heating rates for TGA oxidation versus actual combustion, we are left to wonder: what is the true applicability of this parameter to the comparative instantaneous oxidation of combustion? At combustion timescales, S is predicted to reach negative values

because of the log dependence on heating rate, yet by definition *S* should never be negative (it is a product of only positive numbers). If we assume that *S* merely asymptotically approaches zero with increasing heat rate, then two conclusions about *S* emerge. First, the dependence of *S* on heating rate negates the utility of comparing data on various fuels across the literature that are often taken with different heating rates. Second and more relevant to the present work, all fuels would yield the same *S* values at combustion timescales, and therefore be "equally valuable" as solid fuels, which we know to be false in general. Certainly, an anthracite coal is a "better fuel" than a raw biomass like wood chips. This suggests that *S* is not an appropriate indicator of biomass-based combustion behavior.

5 Rate-limiting timescale analysis

We use first-order scaling analyses to help explain the source of the sensitivities of key rate-limiting timescales to surrounding temperature and oxygen mole fraction. This analysis not meant to serve as a realistic model for the ignition process, but instead to identify the relative timescales of each of the rate-limiting processes from first principles and, more importantly, to understand their sensitivity to the two operational parameters in this study: surrounding temperature and oxygen mole fraction. Figure 13 shows a conceptual model of the combustion process of solid cellulose particles and identifies the key rate-limiting processes that drive the ignition delay and volatile burnout times. The first process is mixing of the hot co-flow gas with the cold N_2 stream that carries the particles. Once the hot co-flow has mixed with the N_2 carrier gas, then the cellulose particles are heated by the gases. Particle heating is followed by devolatilization and ignition delay of the gaseous volatiles. The timescales of these steps determine the ignition delay time. The particle completes its devolatilization process in the presence of the volatile flame and then the remaining volatiles complete combustion. This process is confirmed – albeit at a longer time scale – by the TG results inFigure 10, where we see that the particles experience minimal mass loss at lower temperatures, then devolatilize (and volatiles oxidize) and finally through char/fixed carbon oxidation.

In the remainder of this section, we discuss the timescales associated with each of these processes to explain the measured results presented in Figure 5, Figure 8, and Figure 9 and evaluate the extent to which TG results may mirror the combustion studies. Note that many of these processes overlap in time to an extent that is not possible to estimate without a high-fidelity simulation, which is outside the scope of this study. The following scaling analyses are used for

the purposes of understanding the impact of surrounding temperature and oxygen mole fraction on each of these steps rather than faithfully modeling the cellulose combustion process.

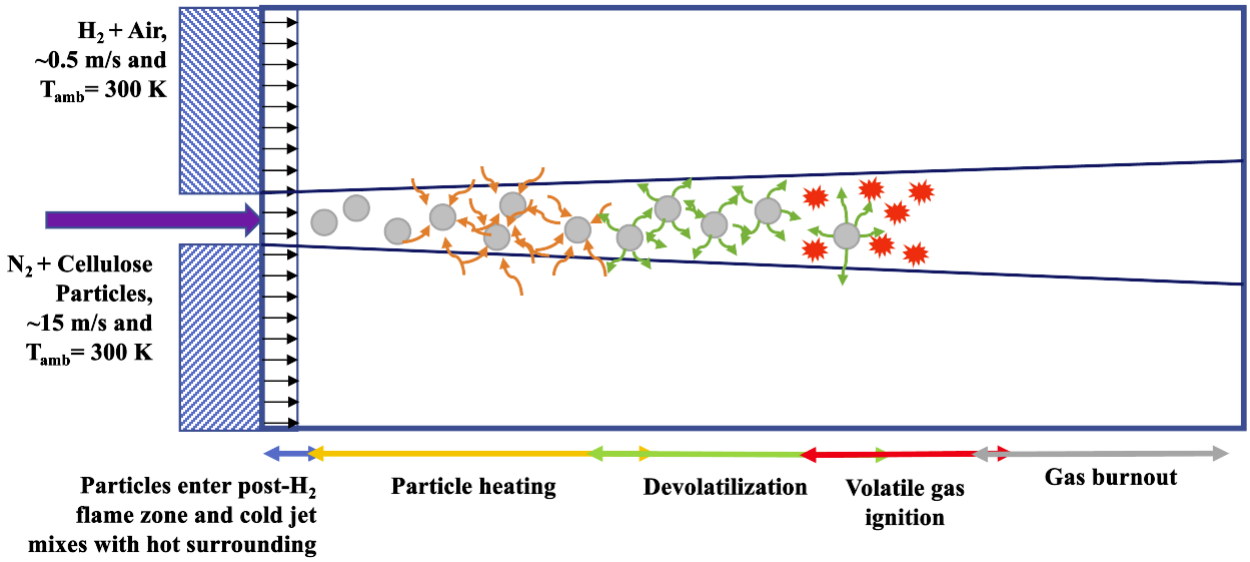

Figure 13. A conceptual model of the combustion process of solid cellulose particles

5.1 Gaseous mixing timescale

The gas mixing process is modelled using the similarity solution for a round jet in a quiescent atmosphere, as in Eqs. 6-11 [63]. The bulk velocity of the nitrogen jet carrying the particles is 8.2 m/s, whereas the co-flow velocity of hot products is 0.32 m/s, making the quiescent assumption a reasonable one for this calculation. A Prandtl number (*Pr*) transformation is used to convert the velocity mixing length from the similarity solution to a temperature mixing length, where *Pr*=0.71 is used for nitrogen. In this formulation, V is the bulk flow velocity, v is the kinematic viscosity of air, and x is the downstream coordinate, which is normalized to η in the similarity solution.

$$f''' + ff'' - \alpha_3 f'^2 = 0 \tag{6}$$

With the boundary conditions: (7)

$$\eta \to -\infty: f' = 0; \eta = 0: f = 0; \eta \to +\infty: f' = 0$$

$$V = \frac{K}{48\nu} \tag{8}$$

$$u = 0.4543 \left(\frac{K^2}{\nu x}\right)^{1/3} (1 - tanh^2\eta) \tag{9}$$

$$v = 0.5503\left(\frac{K\nu}{x^2}\right)^{1/3}[2\eta(1-tanh^2\eta)-tanh\,\eta] \tag{10}$$

$$\eta = 0.2753\left(\frac{K}{\nu^2}\right)^{1/3}\frac{y}{x^{2/3}} \tag{11}$$

The mixing timescale is estimated as the time at which the centerline temperature is 99% of that of the co-flow temperature. Figure 14 shows the gas mixing timescale as a function of co-flow temperature. In all cases, the central jet is assumed to have a temperature of 300 K, or room-temperature nitrogen. As the temperature increases, the thermal mixing timescale also changes, a result of the change in Prandtl number. Note that this timescale is not sensitive to the composition of the co-flow products, only their temperature, and so O_2 concentration has no effect on the gas mixing timescale. The mixing timescales are very fast, on the order of fractions of a millisecond, which is two orders of magnitude shorter than the measured ignition delay times shown in Figure 5, Figure 8, and Figure 9. As such, the gas mixing timescale does not add significantly to the ignition delay of the particles. Recent x-ray mixing experiments by Meng et al. [64] in a similar Hencken burner configuration confirm the rapid mixing times between the central jet and the surrounding hot gases.

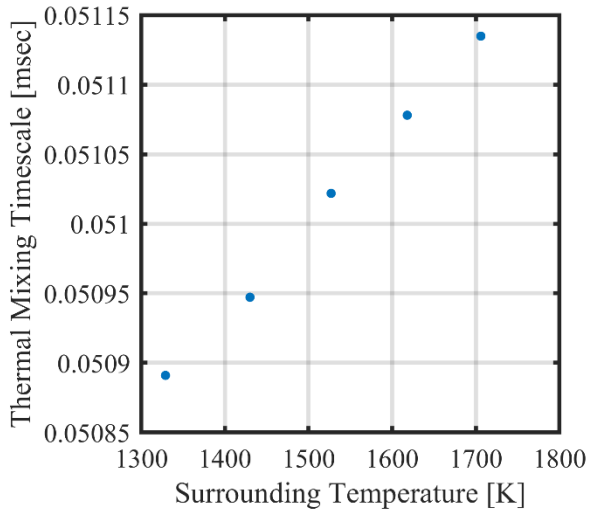

Figure 14. Thermal mixing timescale as a function of surrounding gas temperature.

5.2 Particle heating and devolatilization timescales

The particle heating timescales are estimated using a one-dimensional unsteady conduction solution, as shown in Eq. 12. We assume that the particles are spheres with a diameter of 36 microns, a density of 1440 kg/m^3, a thermal conductivity of 0.04 W/m-K, and a specific heat capacity of 1800 J/kg-K [65,66]. Conductive heat transfer is assumed to be the dominant mode of heat transfer because the Stokes number, $Stk = \rho_p d_p u_g / 18\mu_g$, of the particles is quite small, where *Stk* = 51.23. A small Stokes number indicates that the slip velocity between the particles and the surrounding air is small and so convective heat transfer has a relatively minor effect.

$$\frac{1}{r^2}\frac{\partial}{\partial r}\left(r^2\frac{\partial T}{\partial r}\right) = \frac{1}{\alpha}\frac{\partial T}{\partial t} \tag{12}$$

The conduction timescale is estimated as the time at which the center of the particle reaches 99% of the co-flow temperature. Figure 15a shows the conduction timescale as a function of co-flow temperature for the range of temperatures relevant to this problem. For temperatures this high, the conduction timescale is relatively insensitive to temperature. However, increasing the surrounding temperature increases the conduction timescale because the heat takes slightly longer to raise the particle to a higher temperature given a constant initial particle temperature. This computational observation is confirmed by the TG analysis in Figure 10; increasing the heating rate generates a lag in mass loss (presumably due to conduction within the sample mass given the small particle size and therefore small Biot number).

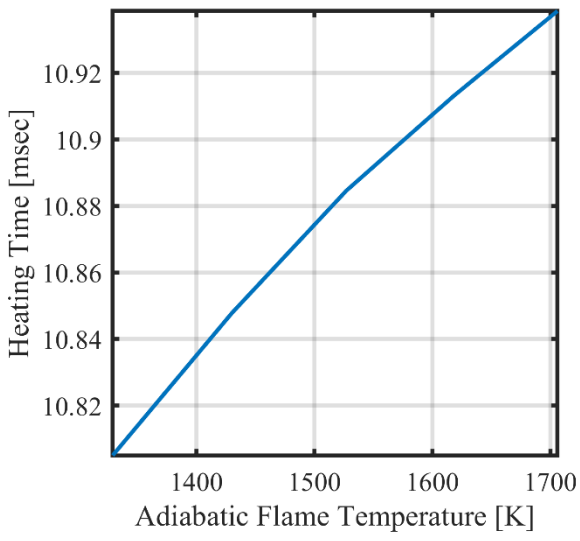

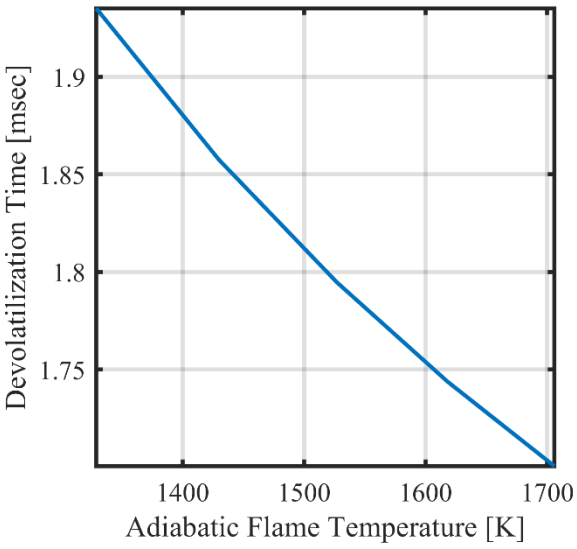

(a) **(b)**

Figure 15. Conduction timescale as a function of co-flow temperature for (a) a center temperature equal to the adiabatic flame temperature and (b) devolatilization timescale.

This analysis assumes that the particle does not devolatilize during the heating process, which is likely not a good assumption. The TG analysis in Figure 10 shows that cellulose begins to devolatilize around 550 K, which is much lower than the co-flow temperatures present in this system. To account for this low-temperature devolatilization, we calculate the devolatilization timescale as the time at which the center of the particle reaches the devolatilization temperature, 550 K, using the same unsteady conduction problem. In this analysis, we assume that devolatilization happens instantaneously upon reaching the devolatilization temperature. This assumption is based on the very rapid mass loss in the TGA pyrolysis experiments shown in Figure 10; however, it is a not realistic and a current drawback of this first-order analysis. Figure 15b shows the devolatilization timescale as a function of co-flow temperature. The devolatilization timescales are an order of magnitude shorter than the calculated conduction timescales in Figure 15a because the temperature that the center must be reached is much lower. Additionally, the timescale decreases with increasing surrounding temperature for a given initial temperature because the heat conduction occurs more quickly with a higher temperature gradient. That said, differences in devolatilization timescales across the temperatures considered in this study are relatively small.

Comparing the devolatilization timescales and the measured ignition delay times in Figure 5, Figure 8, and Figure 9, the heating times are now on the order of the shortest ignition delay times in these experiments, particularly those in air (Figure 5). This result indicates that the time it takes for the particle to devolatilize can be a significant rate-limiting timescale of the cellulose combustion process.

5.3 Gaseous ignition delay and burnout times

The ignition delay time of the gaseous volatiles is a function of both the oxygen mole fraction and the temperature of the surrounding gases. To quantify the ignition delay timescale, we solved for autoignition in a homogeneous reactor in Chemkin-Pro using the AramcoMech 2.0 mechanism [67]. The composition of the gaseous volatiles was approximated from previous data of Hubble and Goldfarb [68], who measured the composition of volatile gases during the temperature ramp

of a thermogravimetric analysis using online gas chromatography mass spectroscopy (GCMS) connected to a TG. Seven species were identified through GCMS during the heating experiment – H_2, N_2, CH_4, H_2O, C_2H_6, O_2, and CO_2 – and signals for each species were summed throughout the experiment to estimate the relative concentration of each of these species in the volatile gases. This method provides a rough estimate of the composition and has many limitations. First, the signals were only considered for channels where the signals for one species did not overlap with other species; thus, the concentration of any given species is likely underestimated. Second, we limited the number of species analyzed to the seven that were measured in this, although many other species are likely present in the volatile gases of cellulose. Finally, the results from Hubble and Goldfarb show that the species mole fractions vary in time as the devolatilization process releases different species at different times; this is not accounted for in this analysis. Given the significant assumptions made in order to estimate the ignition delay times of the volatile gases of cellulose, we perform three compositional sensitivity studies to understand the impact of composition on the results. The results of this sensitivity study are provided in the supplementary material. The baseline composition for the simulations is provided in Table 5.

Table 5. Volatile gas composition for ignition delay time calculations.

Species	**H_2**	**N_2**	**CH_4**	**H_2O**	**C_2H_6**	**O_2**	**CO_2**
Mole Fraction	0.080842	0.512602	0.091673	0.022833	0.003504	0.003427	0.285119

The ignition delay time of the volatiles was estimated using the same process as that from O'Connor et al. [69] for diesel injection; the reader is encouraged to refer to this paper for a complete discussion of the method as well as validation steps taken to understand its applicability. A homogeneous reactor model in Chemkin-Pro is used to calculate the ignition delay time of the mixture in Table 5 at a range of equivalence ratios for the oxidizer compositions and temperatures of the test matrices outlined in Table 1 and Table 2. The composition and temperature of the oxidizer is taken from an equilibrium calculation of the H_2/air flame at the various operating conditions in Table 1 and Table 2, calculated using the Lawrence Livermore hydrogen mechanism [70]. The adiabatic flame temperature is used as the initial temperature of the mixture in the reactor and the composition is limited to the following species – H_2, H_2O, N_2, O_2, OH – because they had orders of magnitude higher mole fractions than the other species considered in the mechanism.

Because the local equivalence ratio distribution of the volatile/oxidizer mixture is not known in the region of the particle, the ignition delay time for a range of equivalence ratios from 0.2 – 2 is calculated at each condition. It is assumed that the mixture that has the shortest ignition delay time is the "most ignitable mixture" and represents the mixture whose ignition would be detected by CH* chemiluminescence imaging in the experiment. While it is clear that ignition in the experiment is not occurring like a homogeneous reactor, this method of estimating ignition delay time from a range of reactor calculations at various equivalence ratios was shown to be highly informative in O'Connor et al. [69] and so is repeated here to provide a first-order estimation of the trends in ignition delay time for cellulose at these different atmospheric conditions.

Ignition is defined as the point in the simulation where the temperature rise rate is the highest. Figure 16 shows an example calculation of 10 equivalence ratios at an initial mixture temperature of 1308 K and an oxygen mole fraction of 0.12, which is the composition of the H_2/air case for ϕ=0.35. The purple circles indicate the location of the highest gradient in temperature and hence the ignition time of the mixture. In all cases the ignition delay time increases with increasing equivalence ratio, as long as the mixture ignites.

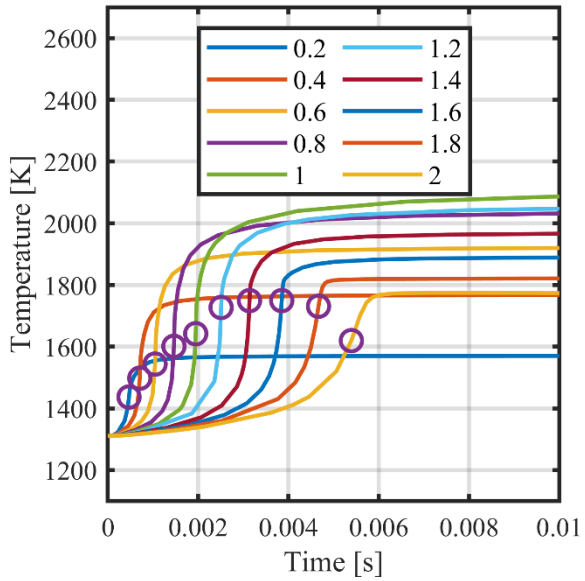

Figure 16. Temperature time histories of 10 equivalence ratios for volatile ignition in the H_2/air case with ϕ=0.35.

The ignition delay times for the three test matrices – constant-temperature, constant-oxygen, and air oxidizer – are shown in Figure 17. Within each test matrix, the ignition delay trends somewhat mirror those of the experiments. For the H_2/air cases, the ignition delay time decreases

as the equivalence ratio of the H_2/air flame increases, increasing the temperature of the surrounding gas. Similarly, in the constant-O_2 cases, the ignition delay time decreases as the temperature of the surrounding gas increases. In the TG results, the ignition temperature increases with heating rate between the 5, 10, and 25 K/min runs (then remains roughly stable thereafter; seeFigure 11). That is, if we heat faster, the T_i is higher because of the conduction heating lag the particle experiences. These results highlight one of the key criticisms of using TG in place of combustion measurements for fuel performance assessment. Not only does the TG significantly underpredict ignition temperature (by a factor of 3), but the timescales for ignition are also significantly overpredicted (by several orders of magnitude; see supplementary material) as a result of the TG heating rate.

Returning toFigure 17, the constant-temperature cases do not provide reliable ignition delay times in the very low-oxygen cases (O_2 mole fractions of 0.01 – 0.04), but then the ignition delay time decreases with increasing O_2 mole fraction in the higher-O_2 cases. However, the trends in ignition delay time across test matrices are opposite those in the actual data (Figure 5 for H_2/air, Figure 8 for constant-temperature, and Figure 9 for constant-O_2), where the H_2/air has the longest ignition delay in simulation but the shortest overall in the experiments.

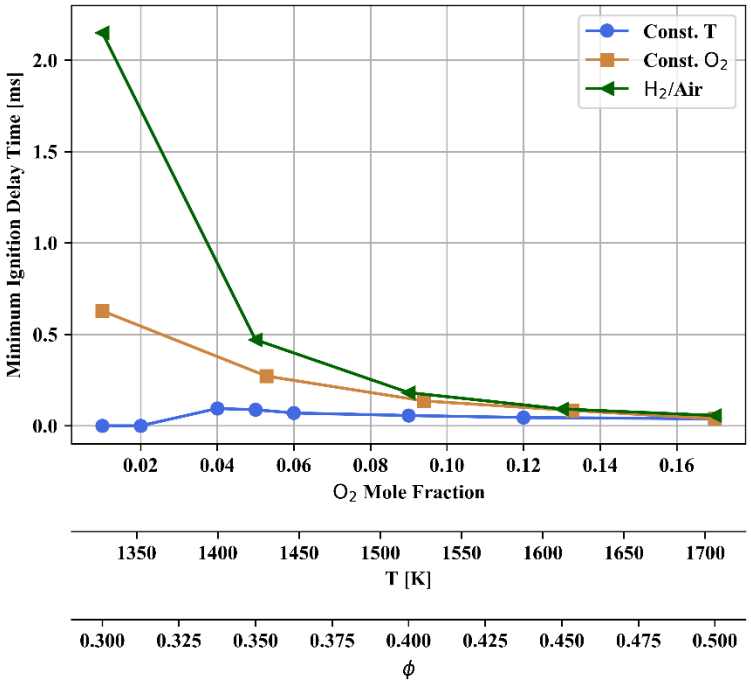

Figure 17. Minimum ignition delay times for three different ignition studies – the constant-temperature, constant-O_2, and H_2/air test matrices.

The reasons for the unreliable calculations at low-oxygen concentrations and the inverse of the overall trends between test matrices can be explained by looking closely at the temperature time histories of each of the cases. Figure 18 shows the temperature time histories for three stoichiometric mixtures at the following conditions – a constant-temperature case (T=1645, O_2=0.04), a constant-O_2 case (T=1527 K, O_2=0.06), and an H_2/air case (T=1308 K, O_2=0.12) – to demonstrate the difference in the exothermicity of the reactions. The low-oxygen, constant-temperature case has a short ignition delay time but also a very small temperature rise – only 343 K as compared to a temperature rise of 537 K for the constant-O_2 case and 793 K for the H_2/air case. While the high starting temperatures of the mixtures partially explains the small temperature rise during the reaction, it is evident that the very low-O_2 cases in the constant-temperature test matrix have very weak heat release; inspection of the heat release rate confirms this as well. This very weak exothermicity is reflected in the experimental results, where low-O_2 cases show high levels of variability in combustion time scales (Figure 8) and a weak flame streak (Figure 7) . As such, it is very difficult to interpret an ignition delay time calculation with such low levels of O_2 and weak exothermicity. Further, the chemical mechanism is likely not validated down to such low levels of oxygen in the oxidizer, making the results rather uncertain.

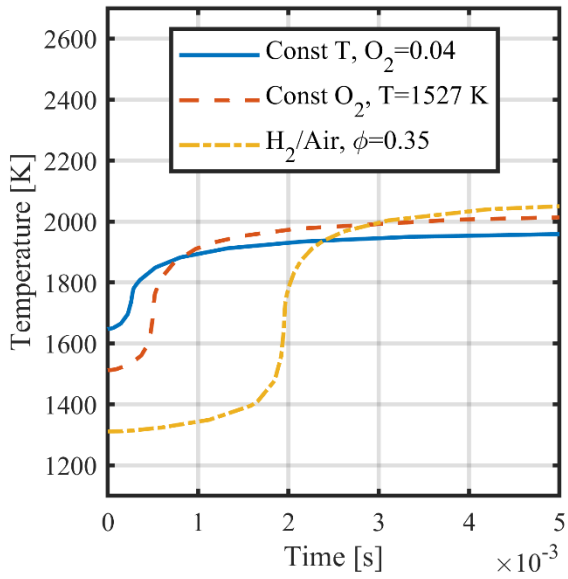

Figure 18. Comparison of temperature time histories of three stoichiometric mixtures in the heterogeneous reactor simulation.

This ignition delay timescale calculation provides an order of magnitude estimate for the ignition delay times for some of the cases where enough oxygen is present to ensure a significant

level of exothermicity. In these cases, the ignition delay times are on the order of 0.1 – 1 millisecond, with variations due to uncertainty in the mixture composition that could result in a range of 0.1 – 10 milliseconds (see supplementary material for composition variation study). These values align closely with those measured in the combustion experiments, as do the trends in a given test matrix, however are orders of magnitude faster than traditional fuel science TG experiments.

6 Conclusions

This study considers the combustion of cellulose in a Hencken burner under three sets of conditions. In the first test matrix, the surrounding gases are the products of an H_2/air flame with varying equivalence ratio, where both oxygen mole fraction and gas temperature vary in opposite directions. The results suggest that the ignition delay time of the cellulose is much more sensitive to temperature than to oxygen mole fraction and that burnout time does not vary significantly with either variable. A test matrix where the flame temperature is maintained at 1645 K and the oxygen mole fraction in the surrounding gases is varied shows that there are two regimes of oxidation – one for very low-oxygen mole fractions (<0.06) where the ignition delay time is very sensitive to oxygen content and one for higher oxygen mole fractions (≥ 0.06) where the ignition delay time is not sensitive to oxygen content. The volatile burnout time shows similar trends, although weaker sensitivities. Finally, a test matrix where the oxygen mole fraction is maintained at 0.06 and the surrounding gas temperature is varied shows that the ignition delay time is highly sensitive to flame temperature, with the volatile burnout time less sensitive.

Measured ignition delay times and their sensitivities to the oxygen content and temperature of the surrounding gases is understood through scaling analysis of the gas mixing time, particle devolatilization time, and volatile ignition delay times. In all conditions, the thermal mixing time is orders of magnitude shorter than any other timescale such that it can be neglected. When summed together, the trends in particle devolatilization time (1-2 ms) and the ignition delay time (0.1-10 ms) align with the results of the measurements well, although the ignition delay time calculations are not reliable for many of the conditions and uncertainty in the volatile composition makes it difficult to interpret results across test matrices.

The results of this study provide three key conclusions from this work. First, the key rate-limiting timescales of cellulose combustion are the devolatilization time and the volatile ignition delay time. Analysis of DTG curves for both inert and oxidative environments showed that the

devolatilization is the same for both environments, indicating that the rapid decomposition of cellulose before ignition is entirely thermally driven and so only dependent on temperature. The ignition delay times are sensitive to both gas temperature and oxygen mole fraction.

Second, the utility of companion DTG and combustion experiments was identified in several parts of this study. The devolatilization temperatures, timescales, and oxygen dependencies could not have been identified in the combustion experiments alone – the data from the DTG were critical to quantifying the devolatilization timescales and sensitivities of cellulose. The so-called Combustion Index (*S* parameter) indicates the dependence of devolatilization regardless of the regime; for the case of cellulose it describes pyrolysis, rather than oxidation. So, while the *S* parameter can be used to describe ignitability and burnout, it cannot be used alone to define the quality of a fuel for combustion applications.

Third, the results at low-oxygen content conditions, in both experiments and chemical simulation, suggest that there are two different regimes of ignition and combustion for conditions with high temperature but low oxygen mole fractions in the oxidizer. These conditions could be critical for final burnout of biomass in industrial systems, and so further investigation of these conditions is warranted. However, adequate chemical mechanisms for describing very low-oxygen conditions may not be available at temperatures relevant to combustion.

Acknowledgements

The authors gratefully acknowledge financial support from National Science Foundation (NSF), grant numbers CBET-2031710 and CBET-2031916. We also thank Jen Colborn for her assistance in creating graphics for the paper.

Declaration of Competing Interest

The authors declare that they have no known competing financial interests or personal relationships that could influence the work reported in this paper.

References

[1] O. Emenike, S. Michailos, K.N. Finney, K.J. Hughes, D. Ingham, M. Pourkashanian, Initial techno-economic screening of BECCS technologies in power generation for a

range of biomass feedstock, Sustainable Energy Technologies and Assessments. 40 (2020) 100743. https://doi.org/10.1016/j.seta.2020.100743.

[2] Y. Liu, M. Geier, A. Molina, C.R. Shaddix, Pulverized coal stream ignition delay under conventional and oxy-fuel combustion conditions, International Journal of Greenhouse Gas Control. 5 (2011) S36–S46.

[3] C. Bu, B. Leckner, X. Chen, A. Gómez-Barea, D. Liu, D. Pallarès, Devolatilization of a single fuel particle in a fluidized bed under oxy-combustion conditions. Part B: Modeling and comparison with measurements, Combust Flame. 162 (2015) 809–818. https://doi.org/10.1016/j.combustflame.2014.08.011.

[4] D. Nutalapati, R. Gupta, B. Moghtaderi, T.F. Wall, Assessing slagging and fouling during biomass combustion: A thermodynamic approach allowing for alkali/ash reactions, Fuel Processing Technology. 88 (2007) 1044–1052. https://doi.org/10.1016/J.FUPROC.2007.06.022.

[5] H. Fatehi, F.M. Schmidt, X.S. Bai, Gas phase combustion in the vicinity of a biomass particle during devolatilization – Model development and experimental verification, Combust Flame. 196 (2018) 351–363. https://doi.org/10.1016/j.combustflame.2018.06.025.

[6] T. Nussbaumer, Combustion and Co-combustion of Biomass: Fundamentals, Technologies, and Primary Measures for Emission Reduction, Energy and Fuels. 17 (2003) 1510–1521. https://doi.org/10.1021/ef030031q.

[7] X. Wang, A. Adeosun, Z. Hu, Z. Xiao, D. Khatri, T. Li, H. Tan, R.L. Axelbaum, Effect of feedstock water leaching on ignition and PM1. 0 emission during biomass combustion in a flat-flame burner reactor, Proceedings of the Combustion Institute. 37 (2019) 2705–2713.

[8] H. Yang, R. Yan, H. Chen, C. Zheng, D.H. Lee, D.T. Liang, In-depth investigation of biomass pyrolysis based on three major components: hemicellulose, cellulose and lignin, Energy & Fuels. 20 (2006) 388–393.

[9] G. Cruz, P.M. Crnkovic, Investigation into the kinetic behavior of biomass combustion under N2/O2 and CO2/O2 atmospheres, J Therm Anal Calorim. 123 (2016) 1003–1011.

[10] D. Vamvuka, S. Sfakiotakis, Combustion behaviour of biomass fuels and their blends with lignite, Thermochim Acta. 526 (2011) 192–199. https://doi.org/10.1016/j.tca.2011.09.021.

[11] E. Boigné, N.R. Bennett, A. Wang, M. Ihme, Structural analysis of biomass pyrolysis and oxidation using in-situ X-ray computed tomography, Combust Flame. 235 (2022) 111737.

[12] A. Williams, M. Pourkashanian, J.M. Jones, Combustion of pulverised coal and biomass, Prog Energy Combust Sci. 27 (2001) 587–610.

[13] R. Khatami, C. Stivers, K. Joshi, Y.A. Levendis, A.F. Sarofim, Combustion behavior of single particles from three different coal ranks and from sugar cane bagasse in O2/N2 and O2/CO2 atmospheres, Combust Flame. 159 (2012) 1253–1271.

[14] Y.B. Yang, H. Yamauchi, V. Nasserzadeh, J. Swithenbank, Effects of fuel devolatilisation on the combustion of wood chips and incineration of simulated municipal solid wastes in a packed bed☆, Fuel. 82 (2003) 2205–2221.

[15] C. Bu, B. Leckner, X. Chen, D. Pallarès, D. Liu, A. Gómez-Barea, Devolatilization of a single fuel particle in a fluidized bed under oxy-combustion conditions. Part A: Experimental results, Combust Flame. 162 (2015) 797–808. https://doi.org/10.1016/j.combustflame.2014.08.015.

[16] P.E. Mason, L.I. Darvell, J.M. Jones, M. Pourkashanian, A. Williams, Single particle flame-combustion studies on solid biomass fuels, Fuel. 151 (2020) 21–30. https://doi.org/10.1016/j.fuel.2014.11.088.

[17] F. Shan, Q. Lin, K. Zhou, Y. Wu, W. Fu, P. Zhang, L. Song, C. Shao, B. Yi, An experimental study of ignition and combustion of single biomass pellets in air and oxy-fuel, Fuel. 188 (2017) 277–284. https://doi.org/10.1016/j.fuel.2016.09.069.

[18] G. Simões, D. Magalhães, M. Rabaçal, M. Costa, Effect of gas temperature and oxygen concentration on single particle ignition behavior of biomass fuels, Proceedings of the Combustion Institute. 36 (2017) 2235–2242. https://doi.org/10.1016/j.proci.2016.06.102.

[19] H. Fatehi, W. Weng, M. Costa, Z. Li, M. Rabaçal, M. Aldén, X.S. Bai, Numerical simulation of ignition mode and ignition delay time of pulverized biomass particles,

Combust Flame. 206 (2019) 400–410. https://doi.org/10.1016/j.combustflame.2019.05.020.

[20] Y.A. Levendis, K. Joshi, R. Khatami, A.F. Sarofim, Combustion behavior in air of single particles from three different coal ranks and from sugarcane bagasse, Combust Flame. 158 (2011) 452–465.

[21] Y. Jia, Z. Li, Y. Wang, X. Wang, C. Lou, B. Xiao, M. Lim, Visualization of Combustion Phases of Biomass Particles: Effects of Fuel Properties, ACS Omega. 6 (2021) 27702–27710.

[22] H. Düdder, A. Wütscher, N. Vorobiev, M. Schiemann, V. Scherer, M. Muhler, Oxidation characteristics of a cellulose-derived hydrochar in thermogravimetric and laminar flow burner experiments, Fuel Processing Technology. 148 (2016) 85–90.

[23] H. Lee, S. Choi, Volatile flame visualization of single pulverized fuel particles, Powder Technol. 333 (2018) 353–363.

[24] G.-M. Kim, J.H. Choi, C.-H. Jeon, D.-H. Lim, Effects of Cofiring Coal and Biomass Fuel on the Pulverized Coal Injection Combustion Zone in Blast Furnaces, Energies (Basel). 15 (2022) 655.

[25] W. Weng, M. Costa, Z. Li, M. Aldén, Temporally and spectrally resolved images of single burning pulverized wheat straw particles, Fuel. 224 (2018) 434–441.

[26] W. Weng, M. Costa, M. Aldén, Z. Li, Single particle ignition and combustion of pulverized pine wood, wheat straw, rice husk and grape pomace, Proceedings of the Combustion Institute. 37 (2019) 2663–2671.

[27] L. Shan, M. Kong, T.D. Bennet, A.C. Sarroza, C. Eastwick, D. Sun, G. Lu, Y. Yan, H. Liu, Studies on combustion behaviours of single biomass particles using a visualization method, Biomass Bioenergy. 109 (2018) 54–60.

[28] S. Wang, C. Zou, C. Lou, H. Yang, M. Mei, H. Jing, S. Cheng, Bioresource Technology Effects of hemicellulose , cellulose and lignin on the ignition behaviors of biomass in a drop tube furnace, Bioresour Technol. 310 (2020) 123456. https://doi.org/10.1016/j.biortech.2020.123456.

[29] H. Fatehi, F.M. Schmidt, X.S. Bai, Gas phase combustion in the vicinity of a biomass particle during devolatilization – Model development and experimental verification,

Combust Flame. 196 (2018) 351–363. https://doi.org/10.1016/J.COMBUSTFLAME.2018.06.025.

[30] H. Yan, O. Fujita, Study of the transient combustion of highly densified biomass briquette (Bio-coke) in an air flow, Fuel. 188 (2017) 595–602. https://doi.org/10.1016/J.FUEL.2016.10.079.

[31] P.E. Mason, L.I. Darvell, J.M. Jones, M. Pourkashanian, A. Williams, Single particle flame-combustion studies on solid biomass fuels, Fuel. 151 (2015) 21–30. https://doi.org/10.1016/J.FUEL.2014.11.088.

[32] F. Shan, Q. Lin, K. Zhou, Y. Wu, W. Fu, P. Zhang, L. Song, C. Shao, B. Yi, An experimental study of ignition and combustion of single biomass pellets in air and oxy-fuel, Fuel. 188 (2017) 277–284. https://doi.org/10.1016/J.FUEL.2016.09.069.

[33] Y.B. Yang, H. Yamauchi, V. Nasserzadeh, J. Swithenbank, Effects of fuel devolatilisation on the combustion of wood chips and incineration of simulated municipal solid wastes in a packed bed☆, Fuel. 82 (2003) 2205–2221. https://doi.org/10.1016/S0016-2361(03)00145-5.

[34] C. Ryu, Y. Bin Yang, A. Khor, N.E. Yates, V.N. Sharifi, J. Swithenbank, Effect of fuel properties on biomass combustion: Part I. Experiments—fuel type, equivalence ratio and particle size, Fuel. 85 (2006) 1039–1046. https://doi.org/10.1016/J.FUEL.2005.09.019.

[35] Y. Jia, Z. Li, Y. Wang, X. Wang, C. Lou, B. Xiao, M. Lim, Visualization of Combustion Phases of Biomass Particles: Effects of Fuel Properties, ACS Omega. 6 (2021) 27702–27710. https://doi.org/10.1021/ACSOMEGA.1C02783/ASSET/IMAGES/LARGE/AO1C02783_0010.JPEG.

[36] W. Weng, M. Costa, M. Aldén, Z. Li, Single particle ignition and combustion of pulverized pine wood, wheat straw, rice husk and grape pomace, Proceedings of the Combustion Institute. 37 (2019) 2663–2671. https://doi.org/10.1016/J.PROCI.2018.05.095.

[37] A. Gani, I.N. Ã, Effect of cellulose and lignin content on pyrolysis and combustion characteristics for several types of biomass, 32 (2007) 649–661. https://doi.org/10.1016/j.renene.2006.02.017.

[38] W. Cao, J. Li, T. Martí-Rosselló, X. Zhang, Experimental study on the ignition characteristics of cellulose, hemicellulose, lignin and their mixtures, Journal of the Energy Institute. 92 (2019) 1303–1312. https://doi.org/10.1016/J.JOEI.2018.10.004.

[39] N.S. Yuzbasi, N. Selçuk, Air and oxy-fuel combustion characteristics of biomass/lignite blends in TGA-FTIR, Fuel Processing Technology. 92 (2011) 1101–1108.

[40] R. Barzegar, A. Yozgatligil, H. Olgun, A.T. Atimtay, TGA and kinetic study of different torrefaction conditions of wood biomass under air and oxy-fuel combustion atmospheres, Journal of the Energy Institute. 93 (2020) 889–898.

[41] J.-J. Lu, W.-H. Chen, Investigation on the ignition and burnout temperatures of bamboo and sugarcane bagasse by thermogravimetric analysis, Appl Energy. 160 (2015) 49–57.

[42] D. Magalhães, F. Kazanç, A. Ferreira, M. Rabaçal, M. Costa, Ignition behavior of Turkish biomass and lignite fuels at low and high heating rates, Fuel. 207 (2017) 154–164. https://doi.org/10.1016/j.fuel.2017.06.069.

[43] J. Li, M.C. Paul, K.M. Czajka, Studies of Ignition Behavior of Biomass Particles in a Down-Fire Reactor for Improving Co-firing Performance, Energy and Fuels. 30 (2016) 5870–5877. https://doi.org/10.1021/acs.energyfuels.6b01065.

[44] A.L. Sullivan, R. Ball, Thermal decomposition and combustion chemistry of cellulosic biomass, Atmos Environ. 47 (2012) 133–141.

[45] A.H. Hubble, J.L. Goldfarb, Synergistic effects of biomass building blocks on pyrolysis gas and bio-oil formation, J Anal Appl Pyrolysis. 156 (2021) 105100.

[46] K. Cheng, W.T. Winter, A.J. Stipanovic, A modulated-TGA approach to the kinetics of lignocellulosic biomass pyrolysis / combustion, Polym Degrad Stab. 97 (2012) 1606–1615. https://doi.org/10.1016/j.polymdegradstab.2012.06.027.

[47] S. Liodakis, D. Bakirtzis, A. Dimitrakopoulos, Ignition characteristics of forest species in relation to thermal analysis data, Thermochim Acta. 390 (2002) 83–91.

[48] J. Cai, Y. He, X. Yu, S.W. Banks, Y. Yang, X. Zhang, Y. Yu, R. Liu, A. V Bridgwater, Review of physicochemical properties and analytical characterization of lignocellulosic biomass, Renewable and Sustainable Energy Reviews. 76 (2017) 309–322. https://doi.org/https://doi.org/10.1016/j.rser.2017.03.072.

[49] D. Shen, R. Xiao, S. Gu, K. Luo, The pyrolytic behavior of cellulose in lignocellulosic biomass: a review, RSC Adv. 1 (2011) 1641–1660.

[50] P. Zong, Y. Jiang, Y. Tian, J. Li, M. Yuan, Y. Ji, M. Chen, D. Li, Y. Qiao, Pyrolysis behavior and product distributions of biomass six group components: Starch, cellulose, hemicellulose, lignin, protein and oil, Energy Convers Manag. 216 (2020) 112777. https://doi.org/10.1016/j.enconman.2020.112777.

[51] P. Kongto, A. Palamanit, P. Ninduangdee, Y. Singh, I. Chanakaewsomboon, A. Hayat, M. Wae-hayee, Intensive exploration of the fuel characteristics of biomass and biochar from oil palm trunk and oil palm fronds for supporting increasing demand of solid biofuels in Thailand, Energy Reports. 8 (2022) 5640–5652. https://doi.org/10.1016/J.EGYR.2022.04.033.

[52] C. Wang, H. Bi, Q. Lin, C. Jiang, X. Jiang, K. Meng, Thermal Characteristics, Kinetics, and Volatility of Co-Combustion of Sewage Sludge and Rice Husk, Bioenergy Res. 14 (2021) 1014–1024. https://doi.org/10.1007/S12155-020-10203-X/TABLES/5.

[53] V. Benedetti, M. Pecchi, M. Baratieri, Combustion kinetics of hydrochar from cow-manure digestate via thermogravimetric analysis and peak deconvolution, Bioresour Technol. 353 (2022) 127142. https://doi.org/10.1016/J.BIORTECH.2022.127142.

[54] C. Wang, F. Wang, Q. Yang, R. Liang, Thermogravimetric studies of the behavior of wheat straw with added coal during combustion, Biomass Bioenergy. 33 (2009) 50–56. https://doi.org/https://doi.org/10.1016/j.biombioe.2008.04.013.

[55] S. Niu, M. Chen, Y. Li, F. Xue, Evaluation on the oxy-fuel combustion behavior of dried sewage sludge, Fuel. 178 (2016) 129–138. https://doi.org/https://doi.org/10.1016/j.fuel.2016.03.053.

[56] S.Y. Luo, B. Xiao, Z.Q. Hu, S.M. Liu, Y.W. Guan, Experimental study on oxygen-enriched combustion of biomass micro fuel, Energy. 34 (2009) 1880–1884. https://doi.org/https://doi.org/10.1016/j.energy.2009.07.036.

[57] Q.H. Nie, S.Z. Sun, Z.Q. Li, X. Zhang, S. Wu, Y. Qi, Thermogravimetric analysis on the combustion characteristics of brown coal blends, Combustion Science and Technology. 7 (2001) 72–76.

[58] G.P. Smith, D.M. Golden, M. Frenklach, N.W. Moriarty, B. Eiteneer, M. Goldenberg, C.T. Bowman, R.K. Hanson, S. Song, W.C. Gardiner Jr., V. V. Lissianski, Q. Zhiwei, GRIMech 3.0, (n.d.). http://combustion.berkeley.edu/gri-mech/.

[59] R.J. Kee, F.M. Rupley, J.A. Miller, M.E. Coltrin, J.F. Grcar, E. Meeks, H.K. Moffat, A.E. Lutz, G. Dixon-Lewis, M.D. Smooke, J. Warnatz, G.H. Evans, R.S. Larson, R.E. Mitchell, L.R. Petzold, W.C. Reynolds, M. Caracotsions, W.E. Stewart, P. Glarborg, C. Wang, O. Adigun, Ansys Chemkin-Pro 2022 R1, (2022).

[60] S. Vyazovkin, K. Chrissafis, M.L. Di Lorenzo, N. Koga, M. Pijolat, B. Roduit, N. Sbirrazzuoli, J.J. Suñol, ICTAC Kinetics Committee recommendations for collecting experimental thermal analysis data for kinetic computations, Thermochimica Acta. 590 (2014) 1–23. https://doi.org/10.1016/j.tca.2014.05.036.

[61] J. Xue, S. Ceylan, J.L. Goldfarb, Synergism among biomass building blocks? Evolved gas and kinetics analysis of starch and cellulose co-pyrolysis, Thermochim Acta. 618 (2015) 36–47.

[62] G.K. Parshetti, A. Quek, R. Betha, R. Balasubramanian, TGA–FTIR investigation of co-combustion characteristics of blends of hydrothermally carbonized oil palm biomass (EFB) and coal, Fuel Processing Technology. 118 (2014) 228–234. https://doi.org/https://doi.org/10.1016/j.fuproc.2013.09.010.

[63] H. Schlichting, J. Kestin, Boundary layer theory, Springer, 1961.

[64] Q. Meng, C. Banyon, A.L. Kastengren, M.S. Wooldridge, R.S. Tranter, Experimental measurement of the rapid mixing of fuel and air in a multi-element diffusion (Hencken) burner, Combust Flame. 251 (2023) 112686.

[65] D. Jones, C. Brischke, Performance of bio-based building materials, Woodhead Publishing, 2017.

[66] C. Sun, True Density of Microcrystalline Cellulose, J Pharm Sci. 94 (2005) 2132–2134. https://doi.org/10.1002/JPS.20459.

[67] W.K. Metcalfe, S.M. Burke, S.S. Ahmed, H.J. Curran, A Hierarchical and Comparative Kinetic Modeling Study of C1 − C2 Hydrocarbon and Oxygenated Fuels, Int J Chem Kinet. 45 (2013) 638–675. https://doi.org/10.1002/KIN.20802.

[68] A.H. Hubble, J.L. Goldfarb, Synergistic effects of biomass building blocks on pyrolysis gas and bio-oil formation, J Anal Appl Pyrolysis. 156 (2021) 105100. https://doi.org/10.1016/J.JAAP.2021.105100.

[69] J. O'Connor, M.P.B. Musculus, L.M. Pickett, Effect of post injections on mixture preparation and unburned hydrocarbon emissions in a heavy-duty diesel engine, Combust Flame. 170 (2016). https://doi.org/10.1016/j.combustflame.2016.03.031.

[70] M. Ó Conaire, H.J. Curran, J.M. Simmie, W.J. Pitz, C.K. Westbrook, A comprehensive modeling study of hydrogen oxidation, Int J Chem Kinet. 36 (2004) 603–622. https://doi.org/10.1002/KIN.20036.